

# Glacial-aged development of the Tunisian Coral Mound Province controlled by glacio-eustatic oscillations and changes in surface productivity

Guillem Corbera<sup>a,b,\*</sup>, Claudio Lo Iacono<sup>c</sup>, Christopher D. Standish<sup>a</sup>, Eulàlia Gràcia<sup>c</sup>, César Ranero<sup>c,d</sup>, Veerle A.I. Huvenne<sup>a</sup>, Eleni Anagnostou<sup>e</sup>, Gavin L. Foster<sup>b</sup>

<sup>a</sup> National Oceanography Centre, Southampton, University of Southampton Waterfront Campus, Southampton SO14 3ZH, United Kingdom

<sup>b</sup> School of Ocean and Earth Science, National Oceanography Centre Southampton, University of Southampton, SO14 3ZH, United Kingdom

<sup>c</sup> Institut de Ciències del Mar (CSIC), Passeig Marítim de la Barceloneta, 08003 Barcelona, Spain

<sup>d</sup> ICREA, Passeig Lluís Companys, Barcelona, Spain

<sup>e</sup> GEOMAR Helmholtz Centre for Ocean Research, Kiel, Germany

## ARTICLE INFO

Editor: Dr Adina Paytan

### Keywords:

Cold-water corals  
Coral mounds  
Mediterranean paleoclimate  
Water mass interface  
Glacial  
Productivity  
Levantine intermediate water  
Laser ablation U–Th dating

## ABSTRACT

Cold-water corals are key species of benthic ecosystems, sensitive to changes in climate and capable of recording them in the chemical composition of their skeletons. The study of cold-water coral mound development in relation to palaeoceanographic variations during the Pleistocene and Holocene stages in the Mediterranean Sea has mainly been focussed in the Alboran Sea (Western Mediterranean). The present study describes the coral deposits and corresponding ages of 3 gravity cores, acquired from the newly discovered Tunisian Coral Mound Province (Central Mediterranean), which comprises several ridge-like mounds. All the cores acquired displayed dense coral deposits, dominated by *Desmophyllum pertusum* fragments embedded within a muddy sediment matrix. Overall, 64 coral samples have been dated with the U–Th laser ablation MC-ICP-MS method, revealing corals of mostly Pleistocene age ranging from ~MIS 11 to 8.4 ka BP. Although coral mound formation was reduced for most of the last 400 kyr, a main stage of pronounced mound formation occurred during the last glacial period, which contrasts to the findings previously published for coral mounds in other regions of the Mediterranean Sea. Coral mound formation during the last glacial was most likely associated with a colder seawater temperature than the one observed in the present-day, an increased surface productivity and an appropriate depth of the interface between Atlantic Waters and Levantine Intermediate Waters. The combination of the data acquired here with that of previous mound formation studies from the Alboran Sea also suggests that cold-water coral mounds located at greater depths develop at slower rates than those found in shallower settings.

## 1. Introduction

Scleractinian cold-water corals (hereafter referred as CWCs) form complex and fragile three-dimensional habitats that enhance the spatial heterogeneity of the seafloor and provide ecological niches for a wide range of species (Henry and Roberts, 2007; Lo Iacono et al., 2018; Price et al., 2019). These biological assemblages are generally found in areas of the continental margins characterised by moderate to strong hydrodynamic regimes, such as submarine canyons, seamounts and ridges (Davies and Guinotte, 2011; Du Preez et al., 2020; Pearman et al., 2020). The strong bottom currents found in these areas provide hard substrates and enhanced food supply that promote CWC settlement and growth

(Fossà et al., 2005; Wheeler et al., 2007). In addition, the physico-chemical conditions of the bathing water-mass (e.g. temperature, pH, dissolved oxygen) play a relevant role in controlling CWC survival and growth (Dodds et al., 2007; Maier et al., 2009; Duineveld et al., 2012; Brooke et al., 2013). However, the environmental range tolerated by the corals seems to be species-specific, with *Madrepora oculata* potentially being able to withstand warmer seawater temperatures than *Desmophyllum pertusum* (synonym = *Lophelia pertusa*, Addamo et al., 2016; Wienberg and Titschack, 2017; Wienberg, 2019). Indeed, in the Mediterranean Sea, CWC assemblages are generally dominated by *M. oculata* (Orejas et al., 2009; Gori et al., 2013; Fabri et al., 2014; Taviani et al., 2017; De la Torre et al., 2018; Corbera et al., 2019), despite the

\* Corresponding author at: National Oceanography Centre, University of Southampton Waterfront Campus, European Way, Southampton SO14 3ZH, United Kingdom.

E-mail address: [guillemcorb@gmail.com](mailto:guillemcorb@gmail.com) (G. Corbera).

<https://doi.org/10.1016/j.margeo.2022.106772>

Received 26 August 2021; Received in revised form 5 March 2022; Accepted 8 March 2022

Available online 16 March 2022

0025-3227/© 2022 Elsevier B.V. All rights reserved.

rather high temperatures observed in situ (i.e.  $\sim 13.9$  °C; Freiwald et al., 2009; Taviani et al., 2017). Nonetheless, these assemblages are still considerably close to their ecological limits regarding water temperature (i.e. 4–14 °C; Rogers, 1999; Brooke et al., 2013).

While extensive CWC assemblages occur throughout the Mediterranean Sea (Chimienti et al., 2019), only a few coral mounds have been discovered in this basin, generally confined to the Alboran Sea (Comas and Pinheiro, 2010; Fink et al., 2013; Lo Iacono et al., 2014; Hebbeln, 2019; Corbera et al., 2019) and the Central Mediterranean (Remia and Taviani, 2005; Taviani et al., 2005; Martorelli et al., 2011; Angeletti et al., 2020). In addition, just some of these mounds host living CWC assemblages in the present: the coral-topped mounds of Santa Maria di Leuca offshore Calabria, Italy (Savini and Corselli, 2010), the Corsica Coral Mound Province located in the Corsica Channel (Angeletti et al., 2020), the exceptionally thriving coral reefs found on the Cabliers Coral Mound Province, in the eastern Alboran Sea (Lo Iacono et al., 2016; Corbera et al., 2019), and the East Melilla Mounds, which present several small and scattered colonies (Fink et al., 2013).

On geological timescales coral mound development generally follows glacial-interglacial cycles, with mound formation occurring either in interglacial (e.g. North American, Irish, Scottish, Norwegian and Namibian mounds; Kano et al., 2007; Rüggeberg et al., 2007; Frank et al., 2011; López Correa et al., 2012; Matos et al., 2017; Tamborrino et al., 2019) or glacial periods (Moroccan and Mauritanian; Wienberg et al., 2010, 2018; Eisele et al., 2011), depending on the environmental setting of their location. However, some South Atlantic mound provinces, such as the Angolan and Brazilian provinces display mound formation both during glacial and interglacial periods (Mangini et al., 2010; Wefing et al., 2017). So far, in the Mediterranean Sea, coral mound formation has been reported to mainly occur during temperate interstadials and interglacial periods (Fink et al., 2012, 2013; Stalder et al., 2018; Wang et al., 2019; Fentimen et al., 2020; Corbera et al., 2021). Although an extensive set of coral ages covering a wide range of regions within the Mediterranean Sea has been acquired by means of U—Th dating, excluding the Alboran Sea, most of these coral ages rely on samples collected from the seafloor surface (McCulloch et al., 2010; Fink et al., 2015; Taviani et al., 2019). These samples allowed to determine that CWCs have grown in the Mediterranean Sea, at least, from the Middle Pleistocene (i.e. 480 ka BP; McCulloch et al., 2010). Yet, the most pronounced coral mound formation stages (i.e. up to  $\sim 400$  cm kyr<sup>-1</sup>) occurred during the Bølling-Allerød (B/A) and the Early Holocene (Fink et al., 2013; Stalder et al., 2015; Wang et al., 2019; Corbera et al., 2021). Furthermore, available studies in this basin have mostly described past coral mound development in the Alboran Sea (Fink et al., 2013; Wang et al., 2019; Fentimen et al., 2020; Corbera et al., 2021), with just one study reporting Holocene coral ages from the Santa Maria di Leuca coral-topped mounds (i.e. Ionian Sea, Fink et al., 2012).

According to the latest findings, coral mound formation during the B/A and Early Holocene in the Alboran Sea has been related to enhanced fluxes of labile organic matter and increased productivity promoted by a more intense gyre circulation (Fink et al., 2013; Stalder et al., 2015, 2018). Another important factor that has been suggested is the depth of the interface between the entering Atlantic Water (AW) and the outflowing Levantine Intermediate Water (LIW), where the interaction between different water-masses likely generates internal waves (van Haren, 2014) that increase vertical mixing, and thus enhance food supply to deeper areas, where the mounds are located (Wang et al., 2019; Corbera et al., 2021). Lastly, Fentimen et al. (2020) associated coral mound formation to enhanced fluvial input during the B/A, which most likely promoted an increase in productivity and provided a sufficient sediment supply for mound aggradation.

The present study describes, by means of U—Th and trace element analyses, the development of three CWC mounds belonging to a recently discovered coral mound province located along the Tunisian continental margin (the Tunisian Coral Mound Province, hereafter referred as TCMP; Fig. 1; Camafort et al., 2020). The TCMP is located off the

northern Tunisian coast and west of the Strait of Sicily, at the intersection between the Western and Eastern Mediterranean basins (Fig. 1). In order to expand our knowledge of the environmental controls on determining coral mound development in the Mediterranean Sea, we aim to: (1) describe part of the temporal evolution of this coral mound province, (2) relate the development of the studied mounds to changes in the local environmental setting, and (3) compare the temporal patterns of mound development observed in this province with those reported in coral mound provinces of the Alboran Sea.

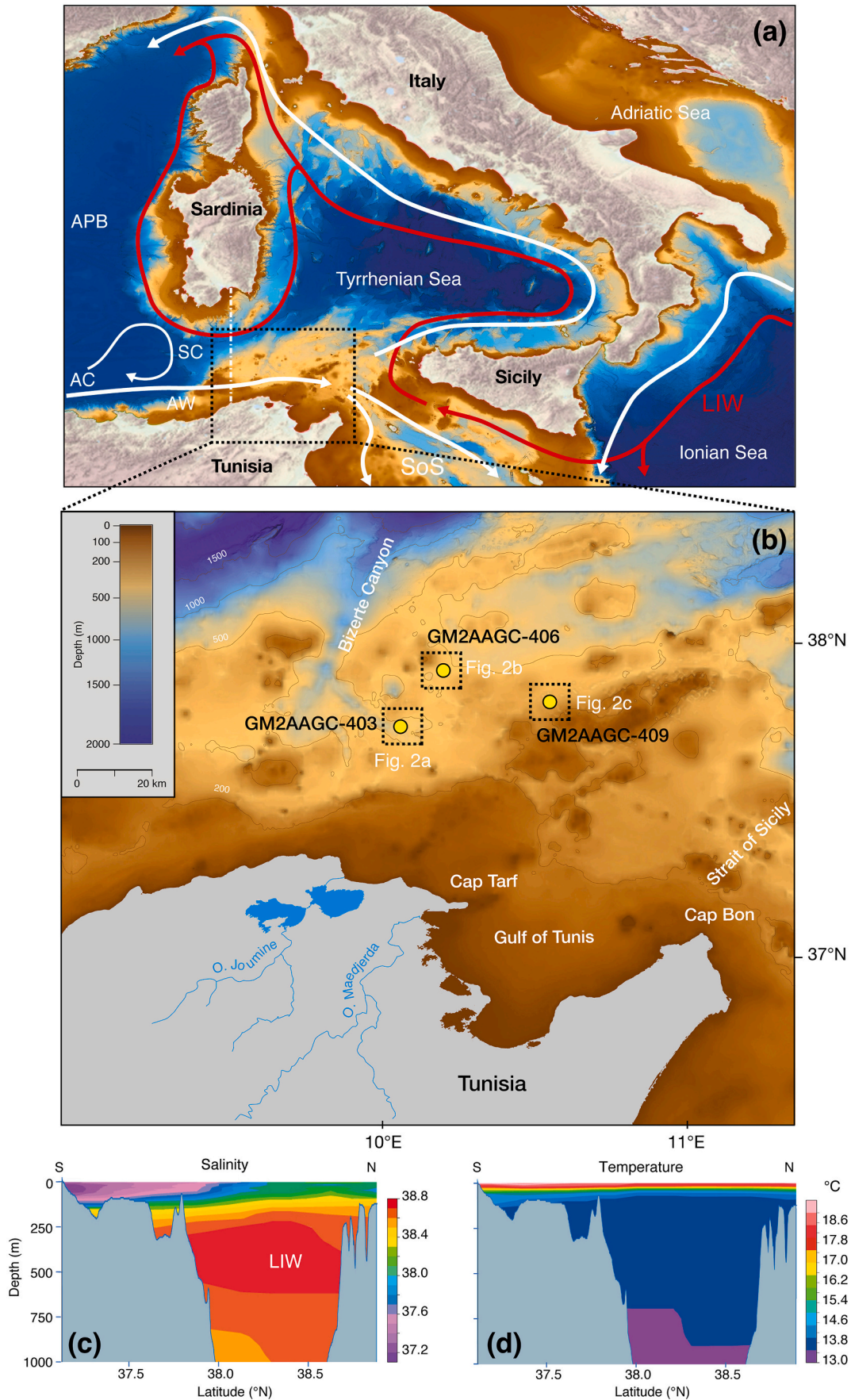
## 2. Geological and oceanographic setting

The TCMP is situated on a plateau cut by the Bizerte Canyon on the northern Tunisian continental slope (South Tyrrhenian Sea; Fig. 1a, b). The plateau is characterised by a complex morphology that consists of a close ridge alignment of parallel ridges and basins that relate to NE-SW trending anticlines and synclines respectively (Masclé et al., 2001). All these features are displaced by NW-SE trending faults, with the Bizerte Canyon being the only landmark that follows a major fault running NE-SW (Fig. 1b; Masclé et al., 2001). The Tunisian Plateau also displays several contourite deposits, mainly reported to the west of the Bizerte Canyon (Camafort et al., 2020). This sector of the Tunisian slope becomes shorter and steeper towards the west and shapes the southern margin of the Sardinian Channel (Fig. 1b). To the southeast, the plateau is bound by the Strait of Sicily (Fig. 1b), which is characterised by a sill of 400 m water depth.

In terms of ocean circulation, the Sardinia-Sicily passage represents an area of key importance within the Mediterranean Sea, as it controls the exchange of water-masses between the Eastern and the Western Basins (Astraldi et al., 2002). The Algerian Current, which flows on the sea surface parallel to the Algerian coast and towards the Tyrrhenian Sea, advects Atlantic nutrient-rich waters all the way from the Alboran Sea at a speed between 10 and 30 cm s<sup>-1</sup> (Fig. 1a, Millot, 1999; Onken et al., 2003; Jouini et al., 2016). Baroclinic instabilities throughout the entire course of the Algerian Current generate anticyclonic eddies, often involving both surface and intermediate waters (Obaton et al., 2000). At the entrance of the Strait of Sicily, the AW splits into two branches, the first flowing along the northern coast of Sicily and the second crossing the strait towards the Eastern Mediterranean Basin (Manzella et al., 1990; Sorgente et al., 2011). In the studied region, the AW occupies the first  $\sim 200$  m of the water column, displaying a salinity core lying around 37.6 psu and a temperature around  $\sim 14$ – $15$  °C (Fig. 1c, d; Gana et al., 2015; Taviani et al., 2017). Below  $\sim 200$  m, where the AW-LIW interface occurs (Ferjani and Gana, 2010), and down to  $\sim 1000$  m the LIW flows in opposite direction at a speed around 5–15 cm s<sup>-1</sup>, from the Strait of Sicily into the Tyrrhenian Sea and through the Sardinian Channel into the Algero-Provençal Basin (Fig. 1a, c; Onken et al., 2003). This water mass is characterised by a salinity core of 38.7 psu and a temperature of  $\sim 13.7$  °C (Fig. 1c, d; Gana et al., 2015; Taviani et al., 2017). In addition, the current speeds of the LIW in the study area might be enhanced due to its proximity to the shallow Strait of Sicily, where they reach up to 50 cm s<sup>-1</sup> (Stansfield et al., 2001).

Increased speeds of westerly winds have been reported on the study area during winter months (i.e. November–March; Soukissian et al., 2018). Such fast blowing winds might cause an strengthening of the Algerian Current and thus, promote the formation of more stable and intense anticyclonic gyres. This would result in increased water column mixing, causing nutrient replenishment in surface waters and thus, enhanced primary productivity throughout winter. Indeed, D'Ortenzio and Ribera d'Alcalà (2009) categorised this region as an oligotrophic area with a well-defined seasonal productivity, characterised by low biomass production during spring-summer and higher productivity throughout autumn and winter.

Sedimentation rates play a key role in coral mound development, as entrapped sediments provide stability to the reef structure, hence allowing mound aggradation. In this regard, Dinarès-Turell et al. (2003)



(caption on next page)

**Fig. 1.** Bathymetric map of the Central Mediterranean Sea (a), with the black dotted rectangle and the dotted white line indicating the location of the TCMP (b) and the vertical hydrographic profiles (c, d) respectively. White and red arrows indicate the circulation patterns of surface (AW) and intermediate (LIW) water masses (Dubois-Dauphin et al., 2017). AW: Atlantic Water, LIW: Levantine Intermediate Water, SC: Sardinian Channel, SoS: Strait of Sicily. (b) Location of GM2AAGC-403, GM2AAGC-406, GM2AAGC-409 gravity cores (yellow dots) on a bathymetric map of the northern Tunisian slope. Salinity (c) and temperature (d) profiles acquired from the World Ocean Atlas 2018 at 0.25° horizontal resolution (Locarnini et al., 2018; Zweng et al., 2019). The Digital Terrain Model at 115 m horizontal resolution has been derived from the EMODnet Bathymetry portal - <http://www.emodnet-bathymetry.eu>. (For interpretation of the references to colour in this figure legend, the reader is referred to the web version of this article.)

defined an almost constant and relatively low sedimentation rate of 2.77 cm kyr<sup>-1</sup> on the Tunisian Plateau (Core LC07, 488 m water depth) during the last 400 kyr, with enhanced Saharan dust supply during glacial periods. Throughout the same period of time, Camafort et al. (2020) described maximum sedimentation rates of 2 cm kyr<sup>-1</sup>, mainly derived from the drift deposits closer to the coast. This indicates that the coral mounds are located in a generally highly energetic and erosive setting.

### 3. Material and methods

#### 3.1. Core acquisition

Three gravity cores (GM2AA-GC403, GM2AA-GC406, GM2AA-GC409) were collected in December 2013 from the summit of different coral mounds located in contrasting regions of the TCMP in terms of water depth (Table 1, Figs. 1b, 2). This survey was carried out on board of the Research Vessel Ramon Margalef from the Instituto Español de Oceanografía (IEO), chartered within the frame of the Geomargen-2 Project by the Institute of Marine Sciences (ICM-CSIC) in collaboration with REPSOL. Core GM2AAGC-403, 234 cm long, was extracted from a ridge-like mound located at the head of one of the branches of the Bizerte Canyon (505 m water depth). The mound extends for 6.4 km in length, rises up to 90 m from the surrounding seafloor, displays flanks with up to 26° of inclination and is accompanied by a series of smaller ridge-like mounds located to the west (Figs. 1b, 2a). Core GM2AAGC-406, 421 cm long, was collected from a ridge-like coral mound at least 11 m tall, located at 475 m water depth and which becomes buried towards the southwest by a layer of sediment up to 6 m thick (Figs. 1b, 2b). This mound extends for >500 m in length and is found several hundreds of meters to the north of a series of ridge-like mounds that occur in a depth range of 450–500 m (Fig. 2b). Core GM2AAGC-409, 78 cm long, was acquired from a ridge-like mound located at 383 m water depth that extends for 3.7 km in length, rises up to 50 m from the surrounding seafloor and presents steep flanks of up to 28° of inclination (Figs. 1b, 2c). GM2AA-GC403, GM2AA-GC406 and GM2AA-GC409 predominantly consist of coral fragments embedded in hemipelagic sediments (Fig. 3). The cores were cut into 1 m sections and frozen prior to being split with a diamond rock saw, which secures that the hemipelagic sediment and the corals embedded in it are kept intact during the splitting process, also minimising coral fragmentation during the cutting process. After splitting, the sections were defrosted, HD photographed by means of a Geotek MSCL-Core Imaging System in the British Ocean Sediment Core Research Facility (BOSCORF). All cores were subsequently visually logged to qualitatively characterise changes in relative coral abundance and species composition along the split surface of the core halves.

**Table 1**

Location, water depth and recovery of the three gravity cores analysed in this study. The U—Th and trace element samples acquired from each core together with the youngest and oldest ages are also indicated.

Core	Lat (°N)	Long (°E)	Water depth (m)	Recovery (cm)	U-Th samples	Li/Mg and Ba/Ca samples	Age (ka BP)	
							Min.	Max.
GM2AAGC403	37.7694070	10.0654777	505	234	22	7	8.39	394.51
GM2AAGC406	37.9496727	10.1927011	475	421	32	6	15.26	85.47
GM2AAGC409	37.8577622	10.5746398	383	78	10	1	14.39	20.86

#### 3.2. Laser ablation U—Th dating

Laser ablation (LA) U—Th analysis offers a ready means to rapidly collect age information on corals collected from coral mound gravity cores, allowing detailed age-depth profiles to be established. The rapidity of the analyses comes however at the cost of precision (LA-based age precisions are larger than typical solution-based analyses). Nonetheless, it is important to note that detailed comparisons between solution and laser ablation techniques (Corbera et al., 2021; Spooner et al., 2016) show that the data generated by LA multi-collector inductively coupled plasma mass spectrometry (LA-MC-ICP-MS) are accurate within the stated uncertainty, and thus is a valid approach to use when solution MC-ICP-MS is not an option. Uranium series techniques were used to date a total of 21, 32 and 10 coral samples acquired from cores GM2AA-GC403, GM2AA-GC406 and GM2AA-GC409, respectively (Table 1), following the methodology outlined in Corbera et al. (2021). Prior to the LA-MC-ICP-MS analyses, samples and standards were mechanically cleaned, mounted in 2.5 cm diameter epoxy resin disks and polished until the surface of the resin was flat and the samples exposed.

LA analyses were performed at the University of Southampton using an Elemental Scientific Lasers (Bozeman, MT, USA) NWR193 excimer laser ablation system with a TwoVol2 ablation chamber coupled to a Thermo Scientific Neptune Plus MC-ICP mass spectrometer (Thermo Fisher Scientific, Waltham, MA, USA). The latter was equipped with nine Faraday cup detectors and an energy filter (Retarding Potential Quadrupole lens) on the central ion counter. Following Spooner et al. (2016), a peak hopping approach was employed, with <sup>230</sup>Th and <sup>234</sup>U intensities measured on the central ion counter and <sup>238</sup>U intensities measured using Faraday cups (Corbera et al., 2021). Integration and idle times of 4.194 s and 1 s were used respectively for both sub-configurations, amounting to a total cycle time of 10.388 s. Solution-based studies have generally only used coral ages associated with <sup>232</sup>Th concentrations below 10 ng g<sup>-1</sup> (Frank et al., 2004), with Krengel (2020) lowering such threshold to 2.5 ng g<sup>-1</sup> for corals younger than 100 ka BP. However, since previous LA-MC-ICP-MS data on CWC shows that age corrections for initial Th based on <sup>232</sup>Th generally fall within the typical age uncertainties for this method (Spooner et al., 2016), measurements of <sup>232</sup>Th were not included in the approach employed here. This decision is further validated by the accuracy of the internal standards discussed below. Typical operating conditions for the laser ablation procedure are detailed in Corbera et al. (2021). Prior to the analyses, sectioned coral samples were ultrasonicated with 18.2 MΩ H<sub>2</sub>O and pre-ablated in order to remove any surface contamination. Laser ablation was performed along a straight line around 2000 μm in length on the sample surface moving at a rate of 10 μm s<sup>-1</sup> (two ablation passes).

Data were collected over 40 analytical cycles. An on-peak gas blank was analysed before and after ablation (both 10 cycles), with 5 cycles allowed for sample washout prior to the latter. Blank corrections were

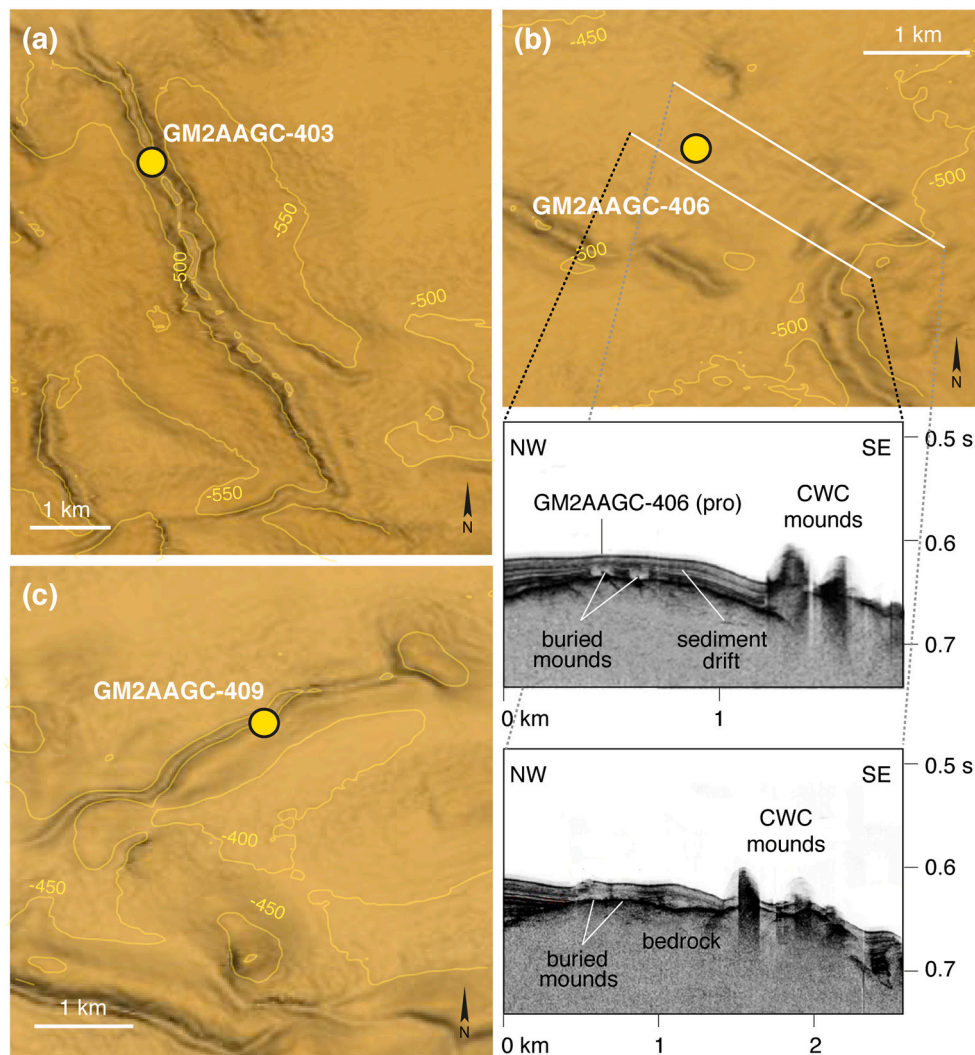


**Fig. 2.** Close-up bathymetric maps of the coral mounds from which the gravity cores GM2AAGC-403 (a), GM2AAGC-406 (b), GM2AAGC-409 (c) were acquired. The white lines in (b) indicate the location of the TOPAS multiparametric echo-sounder profiles showed in the inset, where the coral mound from which core GM2AAGC-406 was acquired, can be observed.

applied to all intensities based on the mean of the preceding and succeeding blank measurements. A fragment of inorganically precipitated aragonite vein, VS001/1-A (Kampman et al., 2012), which was shown to be homogenous on a centimetre scale by Spooner et al. (2016), was analysed bracketing every two samples and used to correct for isotopic and elemental fractionation. Resulting ratios for each coral sample were screened and cycles falling outside the  $3\sigma$  of the mean were removed. Lastly, the following decay constants were used for the calculation of activity ratios:  $\lambda_{230} = (9.1577 \pm 0.028) \cdot 10^{-6} \text{ a}^{-1}$  (Cheng et al., 2000),  $\lambda_{234} = (2.826 \pm 0.0056) \cdot 10^{-6} \text{ a}^{-1}$  (Cheng et al., 2000), and  $\lambda_{238} = (1.55125 \pm 0.0017) \cdot 10^{-10} \text{ a}^{-1}$  (Jaffey et al., 1971). Ages were computed iteratively from the activity ratios and employing these half-lives. Coral samples that were dated multiple times are reported as the mean value of the different ages with an uncertainty of  $2\sigma$ .

Following Spooner et al. (2016), age uncertainties for this study were determined based on the relationship between the external reproducibility of CWC samples analysed  $\geq 3$  times and their ( $^{230}\text{Th}/^{238}\text{U}$ ) (Corbera et al., 2021). Calculated age uncertainties (at 95% confidence) give values of  $\sim 0.7$  ka for ages of 0–10 ka,  $\sim 0.9$  ka for ages of  $\sim 15$  ka,  $\sim 5$  ka for ages of 100 ka, and  $\sim 19$  ka for ages of  $\sim 350$  ka. These are comparable to other studies that have used laser ablation MC-ICP-MS (Eggins et al., 2005; McGregor et al., 2011; Spooner et al., 2016). The uncertainty of samples  $>400$  ka could not be characterised following

this approach and thus, such ages were not considered in detail here.

Potential open system behaviour of U–Th coral samples is typically assessed through the  $\delta^{234}\text{U}_i$ , with samples falling  $>10\%$  from the seawater value of 146.8‰ being excluded from discussions (Andersen et al., 2010). However, when the higher uncertainty associated with the  $\delta^{234}\text{U}_i$  measured by LA-MC-ICP-MS (i.e. 20‰ on samples younger than 100 ka BP; Fig. S1) is summed in quadrature with that of seawater  $\delta^{234}\text{U}_i$  values (i.e. combined uncertainty of 22%), only those samples with values outside the range of 124.8‰ to 168.8‰ can be clearly identified as open system in this study. Additional coral fragments were therefore acquired for XRD analyses to investigate whether secondary calcite was present in coral material at certain sampling depths. To further confirm that diagenesis had not impacted the U–Th data within the bounds of the reported uncertainties, each core was assessed for stratigraphic consistency.

The aggradation rates (ARs) of each coral mound formation period were calculated by associating the oldest and youngest ages of each mound formation to the deepest and shallowest samples of such period respectively. Furthermore, the uncertainties of such ages were used to calculate the potentially minimum aggradation rate for each mound formation stage. This calculation produces a range of ARs for each mound development period which, considering the lower precision of the laser ablation technique, provides a conservative estimate of mound

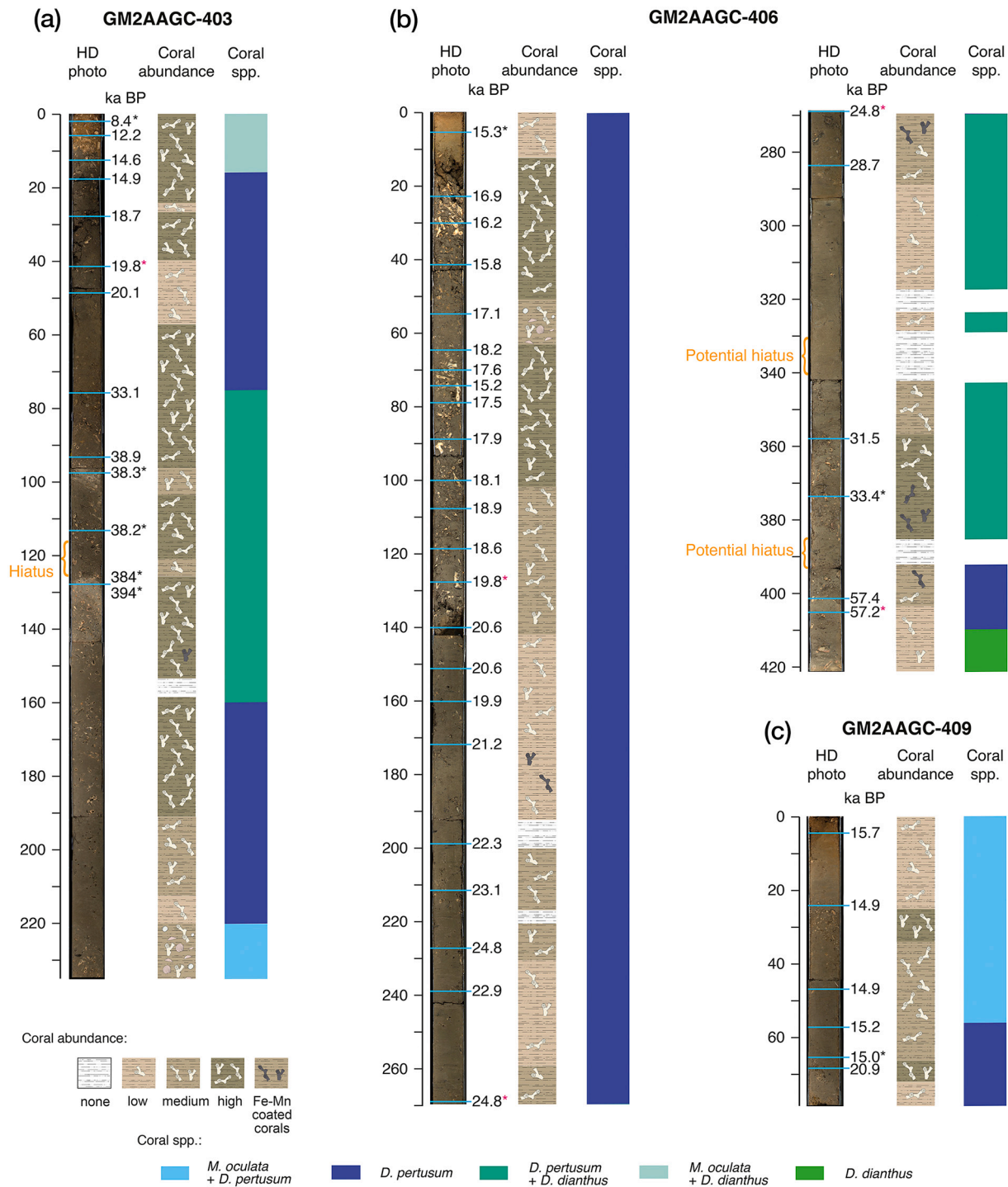


**Fig. 3.** Stratigraphic logs of cores GM2AAGC-403, GM2AAGC-409 (a) and GM2AAGC-406 (b). From left to right: Core HD photo, with location of the coral samples obtained for U—Th dating (blue lines) and their corresponding ages; stratigraphic representation of coral abundance and preservation state; dominant coral species. The asterisk next to some of the coral ages indicate which of the coral samples were also used for trace element analyses, with the red ones denoting trace element data with unrealistic values that are beyond calibration. (For interpretation of the references to colour in this figure legend, the reader is referred to the web version of this article.)

formation pace. Similar to Frank et al. (2009), coral mound formation is associated with ARs >15 cm ky<sup>-1</sup>, whereas lower rates are linked to coral mound stagnation. Age reversals, understood as coral fragments with ages younger than the ones immediately above them, but without any overlap between their uncertainties, are pointed out and discussed for each core.

### 3.3. X-ray diffraction analysis

To confirm that the samples had not been subjected to extensive diagenesis, additional fragments were acquired for XRD analyses (Table S1). Most samples comprised insufficient material to prepare a bulk XRD sample with a standard, instead approximately 100 mg of powder from each was hand ground to a fine powder using an agate

mortar and pestle, prior to being placed on a non-diffracting silicon disc for analysis. Additionally, two samples (a coral and a mineral mixture of aragonite and calcite) comprising 2 g of material were ground in a McCrone Mill for 8 min under isopropanol. The samples were run on a PANalytical X'Pert pro diffractometer machine fitted with a Cu X-ray tube. The machine operating conditions were set at 35 kV, 40 mA utilising automatic slits and a step size of  $0.02^\circ 2\theta$  at 1 s/step. Semi-quantitative analysis of the samples was undertaken using the program Siroquant V4.0 (Sietronics Pty Ltd), an XRD program for phase analysis that uses the "Rietveld" technique. All %error values given are one standard deviation of the total. Siroquant can be used to calculate sample compositions both with and without the addition of a mineral standard.

The precision and accuracy of the coral analyses was verified by a repeat analysis ( $n = 5$ ) of coral sample GM2-GC-403-98 cm (1.5 g) prepared with a corundum spike (25% by weight) and side-loaded to minimize preferred orientation, and a mineral mixture of two standards consisting of 9:1 (aragonite-calcite). The mineral mixture did not include a corundum spike and was run on a silicon disc as a direct methodological comparison. A comparison of the coral sample results run both with and without a standard indicate that the data are within expected levels of precision, as is the accuracy of the 9:1 (aragonite-calcite) mineral mixture ( $\pm 3$  wt%; Hillier, 2000). The data from these two samples are presented in Table S2.

### 3.4. Trace elements

A total of 7, 6 and 1 additional dated corals in cores GM2AA-GC403, GM2AA-GC406 and GM2AA-GC409 were also analysed to acquire Li/Ca, Mg/Ca and Ba/Ca ratios. These fragments were 10–30 mg in mass to average different structural features largely following the sampling approach of others for Li/Mg and Ba/Ca (Spooner et al., 2018; Stewart et al., 2020; Corbera et al., 2021). With the aim of removing any Fe–Mn crust and visible borings, the coral fragments were mechanically cleaned using a circular saw and ultra-sonicated to detach any loose sediments trapped within the coral skeleton. The samples were then subjected to oxidative and reductive cleaning, to eliminate the remaining organic and crustal material (e.g. Barker et al., 2003; Stewart et al., 2020; Spooner et al., 2018) as modified in Corbera et al. (2021). Dissolution occurred with stepwise addition of 0.5 M ultra-pure  $\text{HNO}_3$ .

The Li/Mg ratio is used in CWCs as a proxy for seawater temperature (SWT; Case et al., 2010; Montagna et al., 2014; Stewart et al., 2020). Li/Ca and Mg/Ca ratios in aragonitic marine carbonates are sensitive not only to temperature but also to other environmental parameters, such as seawater carbonate saturation state, and further modified by physiological processes (i.e. vital effects, Fig. S2; Case et al., 2010; Montagna et al., 2014; Marchitto et al., 2018; Stewart et al., 2020). Such overprints in the temperature signal of Li/Ca and/or Mg/Ca ratios appear to be circumvented when looking at the Li/Mg-temperature relationship of aragonitic corals and foraminifera, which appears to be mainly controlled by the temperature-dependent abiotic partition coefficients of Li/Ca and Mg/Ca (Bryan and Marchitto, 2008; Marchitto et al., 2018).

In CWCs the Ba/Ca ratios are linked to seawater Ba concentrations ( $\text{Ba}_{\text{SW}}$ ; Anagnostou et al., 2011; Flöter et al., 2019; Spooner et al., 2018), similarly to foraminifera and tropical corals (e.g. Lea et al., 1989; Lea and Boyle, 1989, 1990; Lea and Spero, 1994; Sinclair, 2005; De Nooijer et al., 2017). Elevated  $\text{Ba}_{\text{SW}}$  and thus Ba/Ca values have traditionally been associated to increased river run-off and melt-water pulses of continental origin, and diffusion from the seafloor and submarine groundwater discharge (e.g. McCulloch et al., 2003; Hall and Chan, 2004; Bahr et al., 2013; Maina et al., 2012; Hoffmann et al., 2014; Cao et al., 2016; Raddatz et al., 2016; Roy-Barman et al., 2019). Additionally, several studies have used Ba/Ca as a proxy to trace changes in pycnocline depth, water mass circulation, upwelling events and nutrient supply in marine carbonates, including CWCs (e.g. Lea et al., 1989; Sinclair, 2005; Raddatz et al., 2014; Bates et al., 2017; Hemsing et al.,

2018; Stewart et al., 2021). Particularly, the  $\text{Ba}_{\text{SW}}$  nutrient-like vertical profile in seawater is linked to Ba adsorption/absorption onto organic particles and its later released at depth through remineralization of organic carbon (e.g. Cardinal et al., 2005; Chan et al., 1977). Therefore, beyond tracing different sources of Ba in seawater and water-masses with distinct  $\text{Ba}_{\text{SW}}$  signatures, Ba/Ca data could also provide information on surface productivity that may act as a food source to CWCs (e.g. Stewart et al., 2021). Nonetheless, to clearly distinguish surface productivity variations from export productivity and water mass changes at depth, further supportive evidence is needed (e.g. Raddatz and Rüggeberg, 2021; Stewart et al., 2021).

A Thermo Scientific Element XR at the University of Southampton, with a long-term precision ( $2\sigma$ ) of in-house consistency standards (matrix-matched synthetic standard solutions) of 2% for Ba/Ca, Mg/Ca, Mn/Ca, Al/Ca and 4% for Li/Ca, was used to measure the elemental ratios through a solution approach, following established protocols (e.g. Rosenthal et al., 1999; Al-Ammar et al., 2000; Babila et al., 2014; Henehan et al., 2015). Here, the most recent multispecies calibration of Stewart et al. (2020) was used to convert Li/Mg ratios into SWT, while the multispecies calibration of Spooner et al. (2018) was employed for  $\text{Ba}_{\text{SW}}$  reconstructions. These calibrations incorporate data from all the species of CWCs used in this study. Due to the long residence time of Li and Mg in the ocean, the changes in the Li/Mg ratio of seawater during the last million years are negligible (Huh et al., 1998) and thus, it can be assumed that seawater Li/Mg ratios did not vary significantly during the timespan encompassed by this study (i.e.  $\sim 400$  kyrs). Even though the Mediterranean Sea corresponds to a high salinity end-member, the Li/Mg ratio appears independent of salinity (Raddatz et al., 2013). Furthermore, no regional effects or off-sets are observed for Li/Mg ratios in coral samples from this basin compared to the global trends (e.g. Montagna and Taviani, 2019).

SWT and  $\text{Ba}_{\text{SW}}$  reconstructions and uncertainties were calculated through the propagation of both the analytical uncertainty of our elemental data and the uncertainty associated to the regression fit of each calibration, refitted using York et al. (2004) in Corbera et al. (2021) and from Stewart et al. (2020), with a Monte Carlo approach ( $n = 1000$ ). The means and standard deviations of the SWT (Stewart et al., 2020) and  $\text{Ba}_{\text{SW}}$  (Spooner et al., 2018) Monte Carlo permutations for each sample are the values used for the subsequent discussion (Table S3).

## 4. Results

### 4.1. Tunisian Coral Mound Province

Based on a rough visual estimation, the recently discovered TCMP consists of up to 160 exposed mounds located within a water depth of 200–670 m. Seismic profiles acquired during the research survey also indicate the presence of contourites and several buried mounds, which increases the number of coral build-ups present in the area. Although some sub-circular mounds are present, most of the coral mounds in this province display a ridge-like morphology that in some cases extends for up to 7 km, with the presence of considerable moats in either one or both sides of the mounds' base. These coral mounds display heights varying from  $\sim 8$  to 100 m, with an average height of  $\sim 40$  m. Although the majority of the mounds are still exposed, their base tends to be buried by several meters of sediment (i.e. up to 46.5 m). Most of the mounds are located on the slope east of the Bizerte Canyon in a 1700 km<sup>2</sup> sector. This sector displays the highest concentration of rocky outcrops and fault scarps, which longitudinal direction coincides with the NNW-SSE and NNE-SSW orientation of the mounds. Nonetheless, several mounds are also present inside the Bizerte Canyon branches and along them.

### 4.2. Core description

#### 4.2.1. Core GM2AAGC-403

This core was acquired from the top of a coral mound at 505 m water

depth (Fig. 2a), and consists of 234 cm of CWC fragments embedded in an olive grey muddy sediment matrix (Fig. 3a). Besides corals, other invertebrates such as bivalves and echinoids are also found within the sediment matrix. The first 11 cm of matrix sediment present a brownish tone, which denotes that oxidative processes have occurred. Below this point, the colour of the sediment changes to olive grey and keeps relatively constant, with only one light grey band at around 126–133 cm core depth (Fig. 3a).

Qualitative visual logging of the core split surface allowed to determine the relative abundance of coral fragments along the core and to identify the main species dominating the coral deposits. 71% of the core length is characterised by the presence of highly dense coral deposits, 14% contains dispersed but still abundant fragments and 13% displays low coral abundance (Fig. 3a). In contrast, only 2% of the core length is characterised by the absence of coral fragments. Most coral fragments throughout the core display a high degree of bio-erosion, and corals with Fe–Mn crusts are observed between 150 and 140 cm core depth (Fig. 3a). Cold-water corals are mainly represented by framework-building species. Although *Desmophyllum pertusum* is the main species observed among the coral fragments, the deepest part of the core (i.e. below 220 cm) consists of a layer formed by a mix of *D. pertusum* and *M. oculata* accompanied by some bivalve shells (Fig. 3a). Similarly, several *Desmophyllum dianthus* individuals are observed between 160 and 75 cm core depth. Lastly, *M. oculata* and the solitary coral *D. dianthus* also occur in the uppermost 16 cm of the core (Fig. 3a).

#### 4.2.2. Core GM2AAGC-406

This core was collected at a depth of 475 m from the top of a > 500 m long ridge-like CWC mound, which becomes buried by a sediment layer of up to 6 m thick towards its southwestern parts (Fig. 2b). Nonetheless, the layer of sediment covering the coral frameworks seems to be drastically reduced in thickness towards the northeast, as the core consists almost entirely (i.e. 421 cm) of CWC and other invertebrates' fragments, embedded in an olive grey muddy sediment matrix (Fig. 3b). Similar to core GM2AAGC-403, the first 15 cm of sediment matrix present a brownish colour that corresponds to oxidative processes and which gradually changes towards grey coloured mud that characterises the rest of the core (Fig. 3b).

Coral fragments present a varying relative abundance throughout the core; 25% of its length presents a high coral abundance, mainly concentrated in the upper 100 cm (Fig. 3b). Below this point, the coral deposits generally display medium (32%) and low (34%) abundance of coral fragments; only 9% of the core length is depleted of coral fragments. In comparison with core GM2AAGC-403, the CWC fragments in this core are in a considerably better state of preservation, with almost no bio-erosion observed on the corals. Nonetheless, several sections of the core contain corals covered with a Fe–Mn crust (400–370 cm, 280–270 cm, 190–174 cm). As for the previous core, most of the coral fragments observed here belong to framework-building species, with *D. pertusum* being the main species observed (Fig. 3b). Some individuals of the solitary coral *D. dianthus* are also observed in the lower half of the core (385 cm and 270 cm), and they become especially abundant in the lowermost 15 cm of the core. Although several bivalve shells are observed throughout the core, a considerable accumulation of these invertebrates can be observed between 65 and 55 cm core depth (Fig. 3b).

#### 4.2.3. Core GM2AAGC-409

This core was acquired from the top of a coral mound at 383 m water depth (Fig. 2c) and consists of 78 cm of CWC fragments embedded in a muddy sediment matrix, which displays a brownish colour until 12 cm core depth and then gradually changes to olive grey (Fig. 3c). In comparison with GM2AAGC-403 and GM2AAGC-406, CWC fragment abundance is relatively low in this core, with only two high abundance intervals in between 25–34 cm and 66–72 cm core depth, equivalent to 19% of the core length (Fig. 3c). The rest of the core is characterised by

one section of medium and two sections of low coral abundance, amounting to 41% and 40% of the core length respectively. Coral preservation is not optimal, as many remineralised fragments are present, especially in the lowermost 10 cm of the core. Most of the coral fragments belong to the framework-building species *D. pertusum*. Nonetheless, several *M. oculata* fragments are observed in the upper 55 cm of the core (Fig. 3c).

### 4.3. Coral mound development

#### 4.3.1. Core GM2AAGC-403

The age-depth model of this core is based on 13 coral samples, following exclusion of 8 samples due to either low aragonite percentages or  $\delta^{234}\text{U}_i$  out of bounds, and ranges from  $394.51 \pm 17.64$  to  $8.39 \pm 0.79$  ka BP (Figs. 4, 5, Table 2). Most of these samples (i.e. 10) correspond to the Marine Isotopic Stage (MIS) 3–2, three of them coinciding with the Last Glacial Maximum (LGM; 26.5–19 ka BP; Clark et al., 2009). From the remaining coral ages, two belong to the MIS 1 interglacial and the last one fits within MIS 11 (Fig. 4a). The latter was analysed several times, yielding two reliable coral ages (i.e. 394 and 384 ka BP) with overlapping errors (Table 2, Fig. 4a). Only one clear mound development stage is observed in this core during the last glacial period, separated from the oldest sample of the core (~384–394 ka BP) by a hiatus that points to a large coral mound stagnation interval of >345 kyr. The  $\delta^{234}\text{U}_i$  values of all analysed samples from this oldest period indicate that most have likely experienced open system behaviour. This, along with the high uncertainty associated with these older ages, means calculating the AR would not be reliable and thus it was not attempted. The main mound formation period extends from ~38.9 to ~8.4 ka BP. Coral mound stagnation starts with the Early Holocene and lasts until the present day (Fig. 5). If the whole period is considered as a continuous mound formation stage, an average AR of  $3.3\text{--}4.0$  cm kyr<sup>-1</sup> is observed. Nonetheless, if an AR is calculated for the 3 LGM ages (~20.1–18.8 ka BP), mound formation reaches a rate of  $5.8\text{--}15.3$  cm kyr<sup>-1</sup>.

#### 4.3.2. Core GM2AAGC-406

In this core, the age-depth model is based on 28 U–Th dated coral samples ranging from  $57.39 \pm 2.78$  to  $15.26 \pm 0.99$  ka BP, as 2 were excluded due to either low aragonite percentages or  $\delta^{234}\text{U}_i$  out of bounds (Figs. 4, 5, Table 2). Almost all the coral ages lie within the last glacial period (i.e. MIS 3–MIS 2), with 11 of them occurring during the LGM. Mound development seems to occur continuously, with the exception of the coral ages ranging from ~57.4 to ~33.4 ka BP, which might represent a period of coral mound stagnation (i.e. AR =  $1.3$  cm kyr<sup>-1</sup>) with sporadic coral growth (Fig. 4a). After this period and coinciding with the end of the MIS 3 and the entire MIS 2, the coral mound starts developing at a faster pace (AR:  $18.03\text{--}21.6$  cm kyr<sup>-1</sup>; Fig. 5). This mound formation stage continued until ~15.2 ka BP, when the mound entered a stagnation stage that is still ongoing (Fig. 5).

#### 4.3.3. Core GM2AAGC-409

The age-depth model for this core comprises 8 coral samples dated through U–Th series, with ages that range from  $20.86 \pm 1.15$  ka BP to  $14.9 \pm 0.97$  ka BP (Table 2, Fig. 5). Two samples were not considered for the age-depth model due to either low aragonite percentages or  $\delta^{234}\text{U}_i$  being out of bounds. All the coral ages fall within the end of the last glacial period (i.e. MIS 2; Fig. 5). A hiatus of ~5 kyr is observed in the coral ages of the deepest part of the core, after which a continuous mound formation stage can be observed (Fig. 5). This period extends from ~15.68 ka BP to ~14.9 ka BP. Nonetheless, its oldest age corresponds with the shallowest sample of the core and thus, caution should be taken when interpreting the calculated AR of  $22.5\text{--}77.5$  cm kyr<sup>-1</sup>.

### 4.4. Paleo-environmental reconstructions

Li/Mg ratios from all the cores present values ranging from 3.2 to 4.5

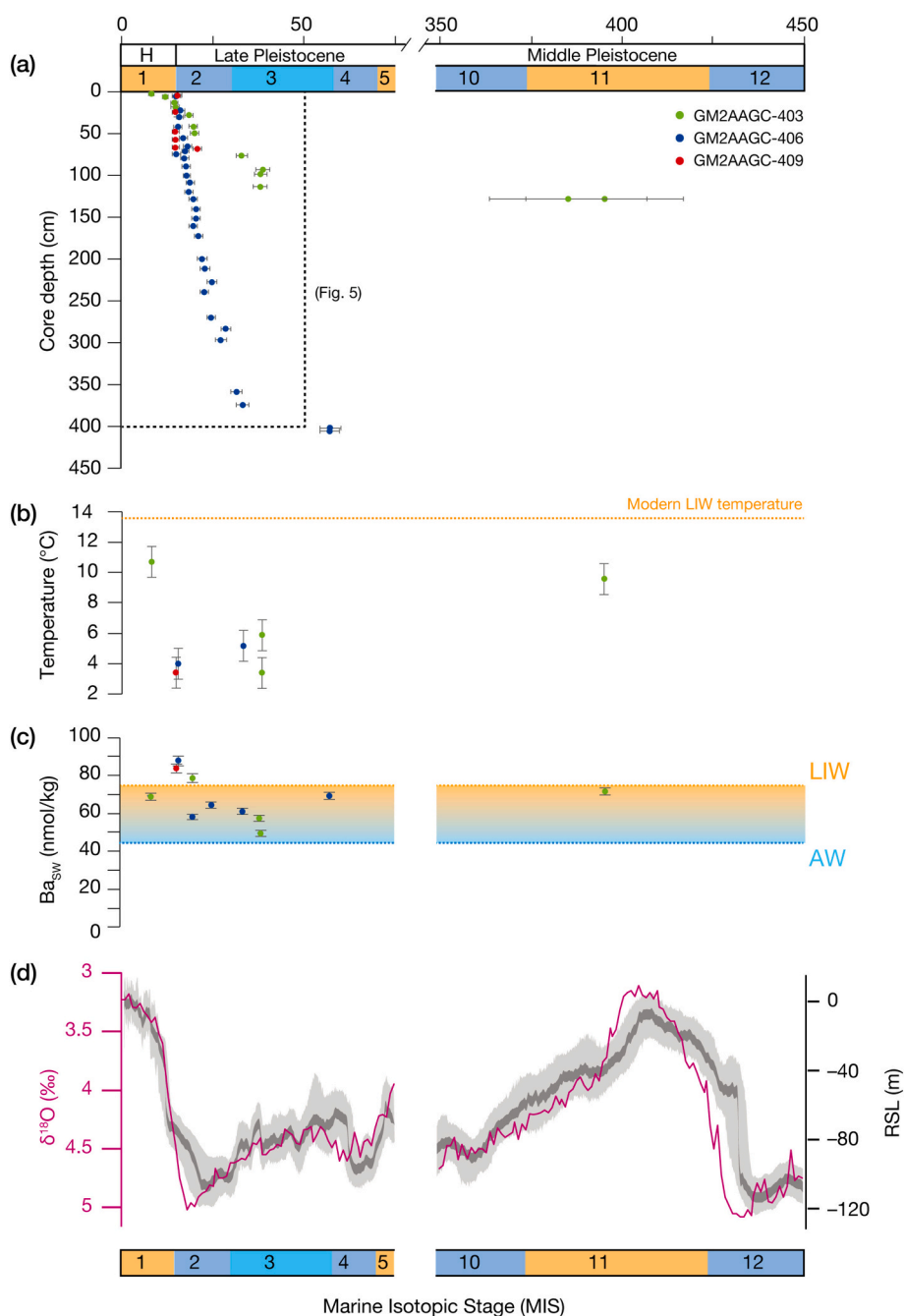


**Fig. 4.** U—Th coral ages (green dots: GM2AAGC-403, blue dots: GM2AAGC-406, red dots: GM2AAGC-409) with associated  $2\sigma$  uncertainties against core depth (a); Sea Water Temperature (SWT) derived from Li/Mg ratios (b);  $Ba_{SW}$  values derived from Ba/Ca ratios (c); LR04  $\delta^{18}O$  (‰) stack data for the last 650 kyr (Lisiecki and Raymo, 2005) and Relative Sea-Level (RSL) dataset from Grant et al. (2014) (d). The orange and blue bars in A indicate interglacial and glacial Marine Isotopic Stages (MIS). The orange and blue dotted lines in (d) show the present-day  $Ba_{SW}$  values of the Levantine Intermediate Water (LIW) and the Atlantic Water (AW). (For interpretation of the references to colour in this figure legend, the reader is referred to the web version of this article.)

$\text{mmol mol}^{-1}$ . The derived SWT values are below the present-day temperature (i.e.  $13.7^\circ\text{C}$ ) and oscillate between  $3.6 \pm 1.2$  and  $10.7 \pm 1.1^\circ\text{C}$  (Fig. 4c; Table S3). From the 14 SWT values acquired through trace element analyses, 5 derived from Li/Mg ratios  $>5.2 \text{ mmol mol}^{-1}$  and were flagged due to their unrealistic values (equivalent to  $<1^\circ\text{C}$ ). This is likely a consequence of the limits of the calibration (Stewart et al., 2020). No obvious pattern exists between these high Li/Mg values and coral Al/Ca and Mg/Ca ratios. In addition, our Mn/Ca ratios are within the range observed in benthic calcitic/aragonitic foraminifera and aragonitic corals after chemical cleaning (e.g. Glock et al., 2012; Fhlaithearta et al., 2010; Drake et al., 2021). Therefore, our low levels of Mn/Ca ratios allow to rule out the presence of significant secondary (i.e. diagenetic) Mn-carbonate or remaining Fe—Mn crustal material after cleaning. This suggests that it is primarily the Li/Ca ratios what causes the issue, as the samples flagged display the highest ratios compared to

the rest of our dataset ( $\geq 14 \mu\text{mol mol}^{-1}$ , Table S3). This is consistent with two of the Alboran sea corals that were excluded from the SWT discussion in Corbera et al. (2021), and could be the result of contamination during analysis. The oldest *D. pertusum* samples (i.e. 394, and 85 ka BP), which correspond with periods of near coral mound stagnation (MIS 11 and 5), show a SWT of  $\sim 9^\circ\text{C}$ . In contrast, during the last glacial period, SWT shows a decreasing trend from  $5.9 \pm 1.1^\circ\text{C}$  in MIS 3 (38.3 ka BP) to  $3.6 \pm 1.2^\circ\text{C}$  in MIS 2 (15.0 ka BP; Fig. 4c). This colder period corresponds with the main mound formation stages observed in all the coral mounds studied in the region (Fig. 4a, c). The youngest sample (i.e. 8.4 ka BP), which lies within the Early Holocene exhibits a SWT of  $10.7 \pm 1.1^\circ\text{C}$ , the highest palaeo-temperature observed in this study (Fig. 4c).

Ba/Ca values from the extracted coral samples range from  $10.2 \pm 0.2$  to  $16.6 \pm 0.3 \mu\text{mol mol}^{-1}$ , resulting in a  $Ba_{SW}$  range of  $49.5 \pm 2.6$  to  $88.0$

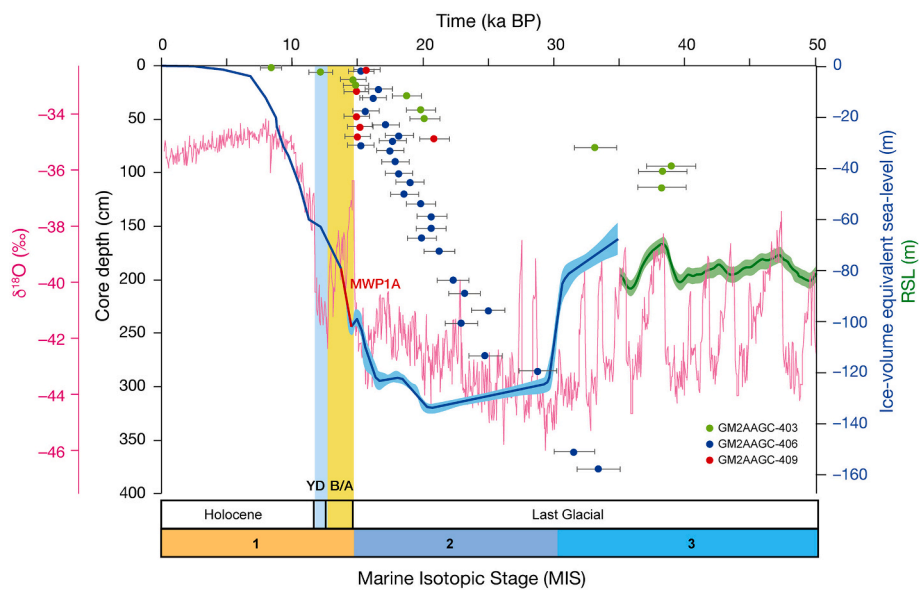


**Fig. 5.** U—Th coral ages (green dots: GM2AAGC-403, blue dots: GM2AAGC-406, red dots: GM2AAGC-409) during the last glacial and Holocene against core depth. Ice-volume equivalent sea-level curve (blue line) from Lambeck et al. (2014), Relative Sea-Level data (green line) from Grant et al. (2014) and NGRIP  $\delta^{18}\text{O}$  (‰) data (purple line) from North Greenland Ice Core Project members, 2004 are also plotted. B/A: Bølling-Allerød, YD: Younger Dryas. (For interpretation of the references to colour in this figure legend, the reader is referred to the web version of this article.)

$\pm 2.7 \text{ nmol kg}^{-1}$  (Fig. 4d, Table S3). Almost half of the samples display  $\text{Ba}_{\text{SW}}$  values within the present-day range of the two Mediterranean Sea end-members (i.e. AW and LIW). Only four samples present higher  $\text{Ba}_{\text{SW}}$  values than those generally observed for the LIW (i.e.  $>70\text{--}75 \text{ nmol kg}^{-1}$ ; Jacquet et al., 2016). These  $\text{Ba}_{\text{SW}}$  values (i.e. 84 and 88  $\text{nmol kg}^{-1}$ ) correspond with the start of the last deglacial period (i.e. 15.0 and 15.3 ka BP, respectively). In contrast, the lowest  $\text{Ba}_{\text{SW}}$  value is observed at 38.3 ka BP, coinciding with the MIS 3.

## 5. Discussion

The main finding of the present study resides in the glacial-aged development of the TCMP coral mounds. Enhanced mound development occurs during the MIS 2 and particularly, since the LGM until the onset of the B/A. However, as it generally occurs with most of the studies aiming to highlight the evolution of coral mounds (Fink et al., 2013; Eisele et al., 2011; Wang et al., 2019; Corbera et al., 2021), the recovery depth of the cores (i.e. 0.8–4.2 m) only allows us to constrain the latest stages of mound formation.

### 5.1. Coral mound development during the Late Pleistocene

Throughout the Middle Pleistocene (773–126 ka BP), sporadic coral growth occurred in the TCMP during  $\sim$ MIS 11. These corals were growing on the coral mound corresponding to core GM2AAGC-403, the westernmost and deepest mound presented here. Following this period, a large hiatus of  $>345 \text{ kyr}$  is present in core GM2AAGC-403, stretching from MIS 10 to 4 and coinciding with a change in sediment colour and a decrease in coral abundance (Figs. 3a, 4a). Such a large hiatus, including entire glacial-interglacial cycles, could be the result of persistent and strong bottom currents that, due to the missing baffling effect provided by growing coral frameworks, prevented the deposition of fine hemipelagic sediments after coral demise (Dorschel et al., 2005). This is supported by the low sedimentation rates observed in off-mound areas throughout the last  $\sim 400 \text{ kyr}$  (Dinarès-Turell et al., 2003; Camafort et al., 2020) and the presence of well-developed moats at the base of the mounds. The other two cores did not recover enough material to determine if the same hiatus occurs in all the sampled mounds presented here.

According to the coral age data set obtained for three of the Tunisian mounds, corals were not present in the TCMP again until the Late Pleistocene (Fig. 4a). During this period, sporadic coral growth

characterised by a *D. pertusum* facies is first observed in the mound corresponding to core GM2AAGC-406 at  $\sim 57 \text{ ka BP}$  (MIS 3; Figs. 3b, 4). It is not until  $\sim 39 \text{ ka BP}$  and  $\sim 33 \text{ ka BP}$  that mound formation starts, as observed in cores GM2AAGC-403 and GM2AAGC-406 respectively (Figs. 3, 5). Except for the slightly enhanced ARs observed during the LGM (i.e.  $5.8\text{--}15.3 \text{ cm kyr}^{-1}$ ), the former core represents a coral mound close to stagnation, with only some sporadic coral growth occurring from  $\sim 38.9$  to  $8.4 \text{ ka BP}$  (Fig. 5). Despite the low formation rates of this mound during the last  $\sim 384 \text{ ka BP}$ , and considering its current height is 90 m, there must have been periods of extremely fast mound development that are not displayed in the GM2AAGC-403 core record. The beginning of mound formation in core GM2AAGC-406 towards the end of MIS 3 is preceded by the occurrence of Fe—Mn coated corals, which most probably indicate that coral skeletons were exposed to seawater for a long time, coinciding either with a mound formation hiatus or extremely intermittent coral growth since  $\sim 57 \text{ ka BP}$  (Fig. 3b). The coral ages of this core relate to a slightly faster mound formation, as the mound develops with an AR of  $18.3\text{--}21.6 \text{ cm kyr}^{-1}$  from  $\sim 33 \text{ ka BP}$  until  $\sim 15 \text{ ka BP}$ . The main mound development period in core GM2AAGC-409 started  $\sim 15.6 \text{ ka BP}$  and lasted until  $\sim 14.9 \text{ ka BP}$ , displaying the fastest mound formation (AR:  $22.5\text{--}77.5 \text{ cm kyr}^{-1}$ ) among all the studied mounds. Nonetheless, it is apparent that all three cores display the highest ARs during the second half of MIS 2, corresponding to the LGM.

Overall, the main mound formation periods of the TCMP occurred during the last glacial period and terminated with the onset of the B/A. Glacial mound formation has also been documented for coral mounds in the temperate NE Atlantic (i.e. off Morocco and Mauritania; Wienberg et al., 2010, 2018; Eisele et al., 2011). This is however an opposite pattern compared to what has been observed in the Alboran Sea (westernmost Mediterranean Sea), where mound formation starts with the onset of the B/A and generally lasts until the Early and Mid-Holocene, with the exception of Northern Cabliers, which still presents thriving CWC reefs (Fink et al., 2013; Stalder et al., 2015; Wang et al., 2019; Corbera et al., 2021). Currently, most of the living CWC assemblages are found in submarine canyons and mounds of the West Mediterranean Basin, within water depths influenced by the LIW (Taviani et al., 2017). Hence, it could be speculated that during the onset of the B/A, the Alboran Sea coral mounds benefited from the transport of coral larvae, via LIW, that might have been produced in submarine canyons and/or the TCMP. Owing to the climatic and oceanographic variations that promoted a more favourable setting for coral growth

Table 2

Laser ablation MC-ICP-MS U—Th results from the Tunisian Mound Province coral samples. Ration within parentheses are activity ratios. i = initial. See Section 3.4. for explanation of the age uncertainties.  $(^{230}\text{Th}/^{238}\text{U})_A = 1 - e^{-\lambda_{230}T} + (\delta^{234}\text{U}_{\text{measured}}/1000) [\lambda_{230}/(\lambda_{230} - \lambda_{234})] (1 - e^{-(\lambda_{230} - \lambda_{234})T})$ , where T is the age.  $\delta^{234}\text{U} = ((^{234}\text{U}/^{238}\text{U})_A - 1) \times 1000$ . Ages in years before present (2019) with propagated uncertainties (2 $\sigma$ ). Ages are uncorrected for initial Th. Samples in italics are characterised by  $\delta^{234}\text{U}_i$  outside the acceptable range for closed-system behaviour and thus, they were not included in the calculation of mean ages or used for coral mound development interpretation. Uncertainties on the  $\delta^{234}\text{U}_i$  are 20‰ for samples under 100 ka BP and 25‰ for older samples. \* Indicates ages removed from figures and discussions due to its aragonite content being <98%.

Core	Depth (cm)	( <sup>230</sup> Th/ <sup>238</sup> U)	2 SE	( <sup>234</sup> U/ <sup>238</sup> U)	2 SE	Ag (ka BP)	2 $\sigma$	$\delta^{234}\text{U}_i$ (‰)
GM2AAGC403	2	0.085	0.010	1.148	0.016	8.39	0.79	151
GM2AAGC403	6	0.122	0.013	1.151	0.017	12.16	0.89	156
GM2AAGC403	13	0.144	0.018	1.143	0.021	14.63	0.96	149
GM2AAGC403	18	0.147	0.028	1.148	0.013	14.86	0.97	154
GM2AAGC403	28	0.181	0.018	1.139	0.016	18.75	1.09	147
GM2AAGC403	41	0.192	0.018	1.145	0.017	19.83	1.13	154
GM2AAGC403	49	0.192	0.012	1.132	0.019	20.12	1.13	140
<i>GM2AAGC403</i>	57	<i>0.264</i>	<i>0.013</i>	<i>1.139</i>	<i>0.015</i>	<i>28.56</i>	<i>1.43</i>	<i>150*</i>
<i>GM2AAGC403</i>	67	<i>0.326</i>	<i>0.025</i>	<i>1.128</i>	<i>0.019</i>	<i>36.85</i>	<i>1.76</i>	<i>143*</i>
GM2AAGC403	76	0.298	0.016	1.128	0.017	33.14	1.60	141
GM2AAGC403	93	0.348	0.027	1.148	0.050	38.93	1.89	166
GM2AAGC403	98	0.340	0.030	1.138	0.030	38.29	1.84	154
GM2AAGC403	113	0.337	0.046	1.131	0.022	38.23	1.82	146
<i>GM2AAGC403</i>	<i>128</i>	<i>1.027</i>	<i>0.032</i>	<i>1.039</i>	<i>0.011</i>	<i>404.76</i>	<i>17.89</i>	<i>122</i>
<i>GM2AAGC403</i>	<i>128</i>	<i>1.017</i>	<i>0.069</i>	<i>1.040</i>	<i>0.018</i>	<i>363.03</i>	<i>17.28</i>	<i>113</i>
<i>GM2AAGC403</i>	<i>128</i>	<i>1.005</i>	<i>0.051</i>	<i>1.036</i>	<i>0.024</i>	<i>345.36</i>	<i>16.60</i>	<i>97</i>
GM2AAGC403	128	1.023	0.047	1.040	0.017	384.34	17.64	118
GM2AAGC403	128	1.032	0.057	1.044	0.022	394.51	18.13	134
<i>GM2AAGC403</i>	<i>133</i>	<i>1.018</i>	<i>0.067</i>	<i>1.035</i>	<i>0.017</i>	<i>388.09</i>	<i>17.33</i>	<i>104</i>
<i>GM2AAGC403</i>	<i>167</i>	<i>1.079</i>	<i>0.142</i>	<i>1.082</i>	<i>0.055</i>	<i>382.75</i>	<i>21.22</i>	<i>244</i>
<i>GM2AAGC403</i>	<i>174</i>	<i>1.012</i>	<i>0.067</i>	<i>1.029</i>	<i>0.019</i>	<i>397.68</i>	<i>17.00</i>	<i>88</i>
<i>GM2AAGC403</i>	<i>192</i>	<i>0.996</i>	<i>0.080</i>	<i>1.035</i>	<i>0.029</i>	<i>327.78</i>	<i>16.09</i>	<i>89</i>
<i>GM2AAGC403</i>	<i>205</i>	<i>1.015</i>	<i>0.097</i>	<i>1.032</i>	<i>0.031</i>	<i>391.11</i>	<i>17.18</i>	<i>98</i>
<i>GM2AAGC403</i>	<i>221</i>	<i>1.024</i>	<i>0.044</i>	<i>1.036</i>	<i>0.016</i>	<i>408.12</i>	<i>17.71</i>	<i>114</i>
<i>GM2AAGC403</i>	<i>221</i>	<i>0.995</i>	<i>0.083</i>	<i>1.039</i>	<i>0.013</i>	<i>317.98</i>	<i>16.08</i>	<i>96</i>
<i>GM2AAGC403</i>	<i>227</i>	<i>1.030</i>	<i>0.062</i>	<i>1.037</i>	<i>0.019</i>	<i>423.96</i>	<i>18.04</i>	<i>124</i>
GM2AAGC406	5	0.152	0.013	1.156	0.013	15.26	0.99	163
GM2AAGC406	22	0.167	0.015	1.158	0.016	16.93	1.04	165
GM2AAGC406	30	0.159	0.017	1.147	0.019	16.19	1.01	154
GM2AAGC406	42	0.156	0.021	1.148	0.025	15.80	1.00	154
GM2AAGC406	55	0.169	0.015	1.157	0.026	17.14	1.05	165
GM2AAGC406	65	0.179	0.021	1.153	0.031	18.23	1.08	161
GM2AAGC406	70	0.171	0.021	1.143	0.035	17.60	1.05	151
GM2AAGC406	74	0.150	0.013	1.148	0.011	15.23	0.98	154
GM2AAGC406	79	0.171	0.018	1.146	0.020	17.48	1.05	153
GM2AAGC406	89	0.173	0.018	1.140	0.020	17.87	1.06	147
GM2AAGC406	100	0.175	0.027	1.133	0.019	18.14	1.06	140
GM2AAGC406	108	0.185	0.014	1.148	0.015	18.99	1.10	156
GM2AAGC406	119	0.181	0.014	1.148	0.016	18.57	1.09	156
GM2AAGC406	128	0.192	0.012	1.145	0.014	19.83	1.13	154
GM2AAGC406	140	0.197	0.019	1.135	0.016	20.64	1.14	143
GM2AAGC406	151	0.198	0.014	1.144	0.016	20.61	1.15	153
GM2AAGC406	160	0.190	0.024	1.131	0.018	19.89	1.12	139
GM2AAGC406	172	0.202	0.014	1.137	0.015	21.23	1.17	145
GM2AAGC406	199	0.212	0.015	1.137	0.022	22.28	1.20	146
GM2AAGC406	211	0.221	0.019	1.147	0.015	23.15	1.24	157
GM2AAGC406	227	0.233	0.018	1.134	0.016	24.85	1.29	144
GM2AAGC406	239	0.219	0.022	1.147	0.028	22.92	1.23	157
GM2AAGC406	269	0.234	0.017	1.146	0.013	24.76	1.30	156
GM2AAGC406	283	0.264	0.015	1.131	0.013	28.74	1.43	143
<i>GM2AAGC406</i>	<i>296</i>	<i>0.253</i>	<i>0.018</i>	<i>1.129</i>	<i>0.023</i>	<i>27.41</i>	<i>1.38</i>	<i>140*</i>
<i>GM2AAGC406</i>	<i>306</i>	<i>0.258</i>	<i>0.073</i>	<i>1.165</i>	<i>0.070</i>	<i>27.07</i>	<i>1.40</i>	<i>178</i>
GM2AAGC406	358	0.286	0.020	1.131	0.020	31.54	1.54	144
GM2AAGC406	374	0.303	0.023	1.141	0.031	33.37	1.63	156
GM2AAGC406	401	0.465	0.027	1.124	0.024	57.39	2.78	146
GM2AAGC406	405	0.466	0.032	1.129	0.024	57.24	2.79	152
<i>GM2AAGC406</i>	<i>415</i>	<i>0.616</i>	<i>0.039</i>	<i>1.118</i>	<i>0.016</i>	<i>85.47</i>	<i>4.58</i>	<i>151*</i>
<i>GM2AAGC406</i>	<i>419</i>	<i>0.613</i>	<i>0.034</i>	<i>1.125</i>	<i>0.016</i>	<i>83.93</i>	<i>4.53</i>	<i>159*</i>
GM2AAGC409	4	0.153	0.014	1.137	0.035	15.68	0.99	143
<i>GM2AAGC409</i>	<i>12</i>	<i>0.147</i>	<i>0.016</i>	<i>1.145</i>	<i>0.023</i>	<i>14.90</i>	<i>0.97</i>	<i>152*</i>
GM2AAGC409	24	0.146	0.016	1.140	0.026	14.89	0.97	146
<i>GM2AAGC409</i>	<i>30</i>	<i>0.143</i>	<i>0.019</i>	<i>1.149</i>	<i>0.023</i>	<i>14.39</i>	<i>0.96</i>	<i>155*</i>
<i>GM2AAGC409</i>	<i>36</i>	<i>0.136</i>	<i>0.018</i>	<i>1.094</i>	<i>0.021</i>	<i>14.40</i>	<i>0.94</i>	<i>98</i>
GM2AAGC409	47	0.148	0.011	1.151	0.023	14.94	0.97	158
GM2AAGC409	57	0.150	0.024	1.149	0.022	15.18	0.98	155
<i>GM2AAGC409</i>	<i>60</i>	<i>0.151</i>	<i>0.015</i>	<i>1.148</i>	<i>0.018</i>	<i>15.25</i>	<i>0.98</i>	<i>154*</i>
GM2AAGC409	66	0.148	0.024	1.148	0.025	15.01	0.98	154
GM2AAGC409	68	0.199	0.020	1.135	0.022	20.86	1.15	143

during this transitional period, such larvae might have eventually been able to settle on the Alboran Sea mounds (Fink et al., 2013; Wang et al., 2019; Corbera et al., 2021).

## 5.2. Paleo-environmental controls on coral mound development

The main period of mound formation in the TCMP, which primarily occurred throughout the MIS 2 cold period, coincides with some of the highest  $Ba_{SW}$  values recorded (65–88 nmol kg<sup>-1</sup>; Fig. 4c). The high MIS 2  $Ba_{SW}$  values could be related to an enhanced aeolian dust supply promoted by the prevailing dry conditions over North Africa during the LGM (Dinarès-Turell et al., 2003; Maher et al., 2010), albeit unlikely sufficient to be the main cause of the  $Ba_{SW}$  increase we observe (e.g. Roy-Barman et al., 2019; Incarbona et al., 2008). Instead, the two highest  $Ba_{SW}$  values (i.e. >80 nmol kg<sup>-1</sup> dating back to ~15–15.3 ± 0.9 ka BP; Fig. 4c), are more likely linked to an enhanced riverine input during the meltwater pulse 1A, which occurred at the onset of the B/A (~14.7 ka BP). Indeed, the Joumine and Medjerda rivers, which originate in the Tell Atlas, end directly south of the TCMP (Fig. 1a) and thus, could have been one of the main causes promoting these  $Ba_{SW}$  maxima during the deglaciation. The study by Raddatz et al. (2016) would also support this hypothesis, as the authors observed a similar  $Ba_{SW}$  pattern throughout the Early Holocene in the coastal CWC reefs off Norway that they attributed to enhanced river run-off during the deglaciation.

Furthermore, comparably to what has been observed in the Alboran Sea (Corbera et al., 2021), the  $Ba_{SW}$  values >70 nmol kg<sup>-1</sup> acquired in the TCMP towards the end of the MIS 2 glacial and the start of Termination 1 could also partly be the consequence of a larger influence of the Ba-enriched LIW in the region (modern LIW- $Ba_{SW}$  ~ 70–75 nmol kg<sup>-1</sup>; Jacquet et al., 2016), caused by a combination of sea-level rise and a shoaling of the LIW axis, due to decreased density of this intermediate water mass (Toucanne et al., 2012; Jacquet et al., 2016). According to Toucanne et al. (2012), the LIW axis started to get deeper practically since the start of the MIS 3 despite the sea-level only oscillated between –60 and –80 m from the current value. This might have brought the AW-LIW interface close enough to the mounds and combined with an enhanced LIW flow and ventilation, it might have allowed the restart of CWC mound formation. Although coral growth is almost continuous during the last glacial, the mound corresponding to core GM2AAGC-403 displays the lowest ARs (3.3–15.3 cm kyr<sup>-1</sup>) and most variable mound formation observed in the province (Fig. 5). Therefore, at least during the last glacial period, it seems that this mound was exposed to less suitable environmental conditions for coral mound development than those experienced by the mounds corresponding to cores GM2AAGC-406 and GM2AAGC-409. GM2AAGC-403 was the deepest core recovered from the TCMP (i.e. 505 m water depth) and thus it represents the development of a mound located further away from the AW-LIW interface than its counterparts (i.e. GM2AAGC-406: 476 m water depth; GM2AAGC-409: 382 m water depth). Water-mass interfaces tend to accumulate and transport organic particles that can be used as food source by the corals (McManus et al., 2003) and thus, coral assemblages found on mounds that are located at a water depth closer to such interfaces can more easily access the organic matter that they contain. In fact, the most pronounced mound formation stages of the TCMP occurred throughout the LGM when the sea level was lowest (–100 to –140 m; Figs. 4, 5) and thus, when the AW-LIW interface was potentially the closest it could be to the mounds' summits. As observed in the grain size and  $\delta^{13}C$  data of Toucanne et al. (2012), this period also coincides with a deepening of the LIW axis (i.e. depth of maximum flow speed) and a ventilation increase from MIS 3 to 2. Such LIW deepening might have placed the AW-LIW interface even closer to the mounds, potentially providing better conditions for CWC growth. Although a couple of MIS 1 coral ages were obtained from the uppermost part of the core GM2AAGC-403, coral mound stagnation in the TCMP seems to coincide with the fastest sea-level rise of the last deglaciation (i.e. Meltwater Pulse 1A event; Fig. 5), when an increase of 20 m in less than

500 years (Lambeck et al., 2014) might have moved the AW-LIW interface too far away from the mounds. These arguments fit with the results acquired by Wang et al. (2019) and Corbera et al. (2021) in the Alboran Sea, where glacio-eustatic oscillations of the AW-LIW interface were linked to regional coral mound development. The presence of sporadic coral growth after the last glacial termination in the mound corresponding to core GM2AAGC-403 could be the result of the enhanced hydrodynamic conditions generally found within submarine canyons (Lopez-Fernandez et al., 2013; Pearman et al., 2020). The intense hydrodynamics together with the funnelling effect observed in canyons tends to translate into increased particle fluxes in comparison to nearby slope settings, which could result in a higher food supply to the corals (DeGeest et al., 2008; Lopez-Fernandez et al., 2013; Wienberg et al., 2018).

In addition to the contrasting temporal pattern of coral mound development observed between the Alboran Sea and the TCMP mounds, the pace at which these features develop in the latter province is also considerably slower (Fig. 6). Tentatively, this might be also related to the depth of the mounds during mound formation. Data shown in Fig. 6 indicate that at the time of maximum mound aggradation rates, Mediterranean coral mounds located at greater depths developed significantly slower than those located on shallower areas ( $R^2 = 0.71$ ,  $p < 0.001$ ). The most thriving mound formation periods of Northern Cabliers, East Melilla and West Melilla coral mounds (average water depth during mound aggradation (WDMA) = 186–359 m), which occurred during the B/A and the Early Holocene, present maximum ARs ranging between 75 and 414 cm kyr<sup>-1</sup> (Fig. 6; Fink et al., 2013; Stalder et al., 2015; Wang et al., 2019; Corbera et al., 2021). In contrast, the potentially fastest mound formation periods of the TCMP (WDMA = 280–431 m) display ARs ranging from ~15 to ~77 cm kyr<sup>-1</sup>, similar to those observed in Southern Cabliers (WDMA = 332 m), which displays a maximum AR of 44 cm kyr<sup>-1</sup> (Figs. 5, 6; Corbera et al., 2021). The data from the different mounds follows a negative exponential curve, which means that the potential effect of the AW-LIW interface on mound ARs increases rapidly towards shallower depths, whereas mound summits located below 375 m water depth display minimal changes in ARs (Fig. 6). Although the pattern of increasing ARs towards shallower depths is evident within each of the two regions, it is statistically significant only in the Alboran Sea (Fig. 6; Alboran Sea:  $R^2 = 0.39$ ,  $p < 0.05$ ; TCMP:  $R^2 = 0.79$ ,  $p > 0.05$ ). The fact that no significant correlation was observed within the Tunisian mounds could be a consequence of the reduced number of cores studied and the small differences in ARs between mounds (Fig. 6).

Furthermore, it is relevant to remark that the particulate organic carbon decay with depth also follows a negative exponential curve (Marsay et al., 2015), which supports our hypothesis on the relation between coral mound formation pace and mounds' water depth. It has to be considered that depth alone does not control mound formation pace, as it is mainly influenced by changes in other environmental variables, such as surface productivity, sedimentation rates and/or hydrodynamic processes that affect the transport of particulate organic carbon towards the mounds. For instance, it is likely that during periods of maximum mound aggradation in each region, surface productivity was higher in the Alboran Sea, as the direct entrance of AW and its complex circulation pattern makes it one of the most productive areas in the Mediterranean (Bosc et al., 2004; Oguz et al., 2014). Similarly, the Alboran Sea also displays higher sedimentation rates than the Tunisian Plateau during periods of maximum mound aggradation (i.e. ~12–20 cm kyr<sup>-1</sup> vs >3 cm kyr<sup>-1</sup>), enhancing coral mound stability and growth (Wang et al., 2019; Dinarès-Turell et al. (2003); Martínez-Dios et al., 2021). Hence, the reduced ARs of the TCMP in comparison to the Alboran Sea coral mounds, during periods of maximum aggradation, are probably caused by a lower food supply to the corals (i.e. less surface productivity and greater water depth of the mounds) and reduced sedimentation rates.

There is additional evidence of the role of surface productivity in the TCMP development during the last glacial from studies on

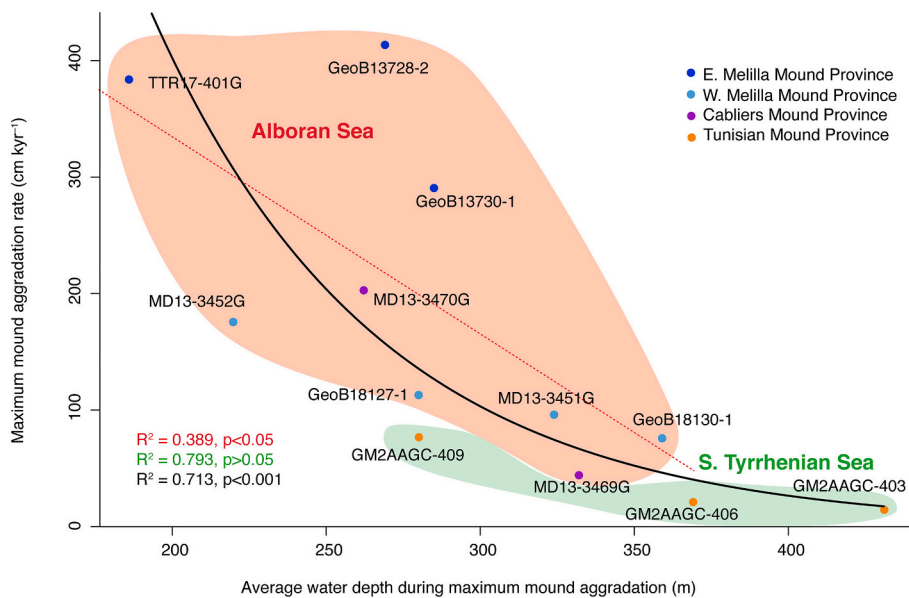


**Fig. 6.** Linear regression models showing the correlation between maximum mound aggradation rates (ARs) and mounds' summit water depth during the time of most pronounced mound formation in the Alboran Sea (red dotted line; East Melilla Mound Province, West Melilla Mound Province and Cabliers Mound Province), the South Tyrrhenian Sea and the Mediterranean Sea as a whole (black line). The ARs have been extracted from Fink et al. (2013), Stalder et al. (2015), Wang et al. (2019) and Corbera et al. (2021). (For interpretation of the references to colour in this figure legend, the reader is referred to the web version of this article.)

coccolithophores, foraminifera and marine biomarkers from the Sardinia Channel and the northern Tunisian Slope (Core LC07). This core revealed the presence of cold and highly productive surface waters during glacial periods (Incarbona et al., 2008; Di Stefano et al., 2015; Martínez-Dios et al., 2021). In the Ionian Sea, Capotondi et al. (2016) described the last parts of glacial periods as being more productive than the start. Considering the proximity between the TCMP and the Ionian Sea, similar changes in productivity might have occurred near the core sites presented in this study. Indeed, such increases in productivity towards the end of glacial periods coincide with the time when the most thriving mound formation stages occurred in this province (Fig. 5). Although the increase in dust supply that occurred during the LGM (Dinarès-Turell et al., 2003) might have helped to fertilize the sea surface with some additional nutrients, according to Incarbona et al. (2008), it is unlikely that such addition was adequate and continuous enough to be the main cause of increased productivity during this period. In contrast, strong westerlies blowing along North Africa (Bout-Roumzeilles et al., 2007) likely caused a strengthening of the Algerian Current that lead to enhanced dynamics of oceanographic features such as eddies (Incarbona et al., 2008; Capotondi et al., 2016). This would have promoted vertical mixing, increasing nutrient supply to the sea surface and ultimately, primary productivity (Cardona and Bracco, 2012).

Besides the low sea level and increased productivity characteristic of glacial periods in this region, SWT was also appropriate for coral growth. Indeed, the main coral mound formation occurred when the reconstructed SWTs ranged between  $3.6 \pm 1.1$  and  $5.9 \pm 1.1$  °C (Table S3, Fig. 4). The modern SWT of the LIW in the study area reaches up to 13.9 °C (Freiwald et al., 2009; Taviani et al., 2017), a value close to the CWCs' physiological limit (i.e. 14 °C; Davies and Guinotte, 2011; Brooke et al., 2013). Hence, it is possible that besides the higher sea-level and productivity decrease, warmer SWTs typical of the Holocene might have also contributed to limit coral growth in the TCMP. Although most of the mounds' records consists of *D. pertusum*, the uppermost section of core GM2AAGC-403 is dominated by *M. oculata* with ages corresponding to the Early Holocene and to a SWT of  $10.7 \pm 1.1$  °C (Figs. 3a, 4). This change in coral facies with increasing temperatures has also been observed in the Alboran Sea (Stalder et al., 2015; Wienberg, 2019; Corbera et al., 2021), as *M. oculata* is known to withstand and prefer higher SWTs than *D. pertusum* (Naumann et al., 2014; Wienberg and Titschack, 2017).

## 6. Conclusions

This study broadens the current knowledge on coral mound formation in the Mediterranean Sea through the description of mound development in the recently discovered Tunisian Coral Mound Province (TCMP; South Tyrrhenian). We conclude that:

- The TCMP is the first Mediterranean coral mound province so far to display mound formation stages during the last glacial period.
- Coral mound formation during cold periods was most likely driven by enhanced surface water productivity combined with an appropriate depth of the AW-LIW interface and a cooler sea water temperature than the one observed in the present-day.
- The increasing ARs from deeper to shallower mounds suggest that, as described in the Alboran Sea, the distance from the AW-LIW interface to the mounds might be key in determining their formation pace.
- In order to confirm the glacial-aged development of the TCMP, to determine the initial settlement of corals and to describe the current ecological state of the province, further studies involving additional cores that drill down to the base of the mounds and Remoted Operated Vehicle (ROV) video- or photo-transects should be performed.

## Data availability

All relevant data used for the research described in this article are included in the article and/or its supplementary files.

## Declaration of Competing Interest

The authors declare that they have no known competing financial interests or personal relationships that could have appeared to influence the work reported in this paper.

## Acknowledgements

Guillem Corbera is funded by the Graduate School of the National Oceanography Centre Southampton (GSNOCS). Veerle Huvenne is supported by the NERC-funded CLASS programme (Grant No. NE/R015953/1) and the EU H2020 programme iAtlantic (Grant No 818123). We are thankful to all the scientists and crew of the Geomargen-2 Cruise for their outstanding work. We are grateful to

Richard Pearce for performing the XRD analysis, along with Andy Milton and Mathew Cooper for their help with analytical aspects of the study and Heather Goring-Harford for her assistance in acquiring a subset of the trace element data. We appreciate the help provided by Suzanne MacLachlan and the British Ocean Sediment Core Research Facility (BOSCORF) team during sampling. We are also grateful to Laura Robinson for supplying the VS001/1-A standard. Lastly, we are thankful to the anonymous reviewers whose comments and suggestions greatly improved this manuscript. The regional Digital Terrain Model data products have been derived from the EMODnet Bathymetry portal - <http://www.emodnet-bathymetry.eu>.

## Appendix A. Supplementary data

Supplementary data to this article can be found online at <https://doi.org/10.1016/j.margeo.2022.106772>.

## References

- Addamo, A.M., Vertino, A., Stolarski, J., García-Jiménez, R., Taviani, M., Machordom, A., 2016. Merging scleractinian genera: the overwhelming genetic similarity between solitary *Desmophyllum* and colonial *Lophelia*. *BMC Evol. Biol.* 16, 1–17. <https://doi.org/10.1186/s12862-016-0654-8>.
- Al-Ammar, A.S., Gupta, R.K., Barnes, R.M., 2000. Elimination of boron memory effect in inductively coupled plasma-mass spectrometry by ammonia gas injection into the spray chamber during analysis. *Spectrochim. Acta, Part B At. Spectrosc.* 55 [https://doi.org/10.1016/S0584-8547\(00\)00197-X](https://doi.org/10.1016/S0584-8547(00)00197-X).
- Anagnostou, E., Sherrell, R.M., Gagnon, A., LaVigne, M., Field, M.P., McDonough, W.F., 2011. Seawater nutrient and carbonate ion concentrations recorded as P/Ca, Ba/Ca, and U/Ca in the deep-sea coral *Desmophyllum dianthus*. *Geochim. Cosmochim. Acta* 75, 2529–2543. <https://doi.org/10.1016/j.gca.2011.02.019>.
- Andersen, M.B., Stirling, C.H., Potter, E.K., Halliday, A.N., Blake, S.G., McCulloch, M.T., Ayling, B.F., O'Leary, M.J., 2010. The timing of sea-level high-stands during Marine Isotope Stages 7.5 and 9: Constraints from the uranium-series dating of fossil corals from Henderson Island. *Geochim. Cosmochim. Acta* 74. <https://doi.org/10.1016/j.gca.2010.03.020>.
- Angeletti, L., Castellan, G., Montagna, P., Remia, A., Taviani, M., 2020. The “Corsica Channel Cold-Water Coral Province” (Mediterranean Sea). *Front. Mar. Sci.* 7, 661. <https://doi.org/10.3389/fmars.2020.00661>.
- Astraldi, M., Gasparini, G.P., Vetrano, A., Vignudelli, S., 2002. Hydrographic characteristics and interannual variability of water masses in the Central Mediterranean: a sensitivity test for long-term changes in the Mediterranean Sea. *Deep. Res. Part I Oceanogr. Res. Pap.* 49, 661–680. [https://doi.org/10.1016/S0967-0637\(01\)00059-0](https://doi.org/10.1016/S0967-0637(01)00059-0).
- Babila, T.L., Rosenthal, Y., Conte, M.H., 2014. Evaluation of the biogeochemical controls on B/Ca of Globigerinoides ruber white from the Oceanic Flux Program, Bermuda. *Earth Planet. Sci. Lett.* 404 <https://doi.org/10.1016/j.epsl.2014.05.053>.
- Bahr, A., Schönfeld, J., Hoffmann, J., Voigt, S., Aurahs, R., Kucera, M., Flögel, S., Jentzen, A., Gerdes, A., 2013. Comparison of Ba/Ca and  $\delta^{18}\text{O}_{\text{WATER18}}$  as freshwater proxies: a multi-species core-top study on planktonic foraminifera from the vicinity of the Orinoco River mouth. *Earth Planet. Sci. Lett.* 383 <https://doi.org/10.1016/j.epsl.2013.09.036>.
- Barker, S., Greaves, M., Elderfield, H., 2003. A study of cleaning procedures used for foraminiferal Mg/Ca paleothermometry. *Geochem. Geophys. Geosyst.* 4. <https://doi.org/10.1029/2003GC000559>.
- Bates, S.L., Hendry, K.R., Pryer, H.V., Kinsley, C.W., Pyle, K.M., Woodward, E.M.S., Horner, T.J., 2017. Barium isotopes reveal role of ocean circulation on barium cycling in the Atlantic. *Geochim. Cosmochim. Acta* 204. <https://doi.org/10.1016/j.gca.2017.01.043>.
- Bosc, E., Bricaud, A., Antoine, D., 2004. Seasonal and interannual variability in algal biomass and primary production in the Mediterranean Sea, as derived from 4 years of SeaWiFS observations. *Glob. Biogeochem. Cycles* 18, GB1005. <https://doi.org/10.1029/2003gb002034>.
- Bout-Roumazielles, V., Combourieu Nebout, N., Peyron, O., Cortijo, E., Landais, A., Masson-Delmotte, V., 2007. Connection between South Mediterranean climate and North African atmospheric circulation during the last 50,000 yr BP North Atlantic cold events. *Quat. Sci. Rev.* 26, 3197–3215. <https://doi.org/10.1016/j.quascirev.2007.07.015>.
- Brooke, S., Ross, S.W., Bane, J.M., Seim, H.E., Young, C.M., 2013. Temperature tolerance of the deep-sea coral *Lophelia pertusa* from the southeastern United States. *Deep Sea Res. Part II Top. Stud. Oceanogr.* 92, 240–248.
- Bryan, S.P., Marchitto, T.M., 2008. Mg/Ca-temperature proxy in benthic foraminifera: New calibrations from the Florida Straits and a hypothesis regarding Mg/Li. *Paleoceanography* 23. <https://doi.org/10.1029/2007PA001553>.
- Camafort, M., Gràcia, E., Ranero, C.R., 2019. Quaternary Seismostratigraphy and Tectonosedimentary Evolution of the North Tunisian Continental Margin. *Tectonics* 39. <https://doi.org/10.1029/2020TC006243>.
- Cao, Z., Siebert, C., Hathorne, E.C., Dai, M., Frank, M., 2016. Constraining the oceanic barium cycle with stable barium isotopes. *Earth Planet. Sci. Lett.* 434 <https://doi.org/10.1016/j.epsl.2015.11.017>.
- Capotondi, L., Girone, A., Lirer, F., Bergami, C., Verducci, M., Vallefucio, M., Afferi, A., Ferraro, L., Pelosi, N., De Lange, G.J., 2016. Central Mediterranean Mid-Pleistocene paleoclimatic variability and its association with global climate. *Palaeogeogr. Palaeoclimatol. Palaeoecol.* 442, 72–83. <https://doi.org/10.1016/j.palaeo.2015.11.009>.
- Cardinal, D., Savoye, N., Trull, T.W., André, L., Kopczynska, E.E., Dehairs, F., 2005. Variations of carbon remineralisation in the Southern Ocean illustrated by the Baxs proxy. *Deep. Res. Part I Oceanogr. Res. Pap.* 52. <https://doi.org/10.1016/j.dsr.2004.10.002>.
- Cardona, Y., Bracco, A., 2012. Enhanced vertical mixing within mesoscale eddies due to high frequency winds in the South China Sea. *Ocean Model* 42, 1–15. <https://doi.org/10.1016/j.ocemod.2011.11.004>.
- Case, D.H., Robinson, L.F., Auro, M.E., Gagnon, A.C., 2010. Environmental and biological controls on Mg and Li in deep-sea scleractinian corals. *Earth Planet. Sci. Lett.* 300, 215–225. <https://doi.org/10.1016/j.epsl.2010.09.029>.
- Chan, L.H., Drummond, D., Edmond, J.M., Grant, B., 1977. On the barium data from the Atlantic GEOSECS expedition. *Deep. Res.* 24 [https://doi.org/10.1016/0146-6291\(77\)90505-7](https://doi.org/10.1016/0146-6291(77)90505-7).
- Cheng, H., Adkins, J., Edwards, R.L., Boyle, E.A., 2000. U-Th dating of deep-sea corals. *Geochim. Cosmochim. Acta* 64, 2401–2416. [https://doi.org/10.1016/S0016-7037\(99\)00422-6](https://doi.org/10.1016/S0016-7037(99)00422-6).
- Chimienti, G., Bo, M., Taviani, M., Mastrototaro, F., 2019. Occurrence and Biogeography of Mediterranean Cold-Water Corals. In: *Mediterranean Cold-Water Corals: Past, Present and Future*, pp. 213–243. [https://doi.org/10.1007/978-3-319-91608-8\\_19](https://doi.org/10.1007/978-3-319-91608-8_19).
- Clark, P.U., Dyke, A.S., Shakun, J.D., Carlson, A.E., Clark, J., Wohlfarth, B., Mitrovica, J. X., Hostetler, S.W., McCabe, A.M., 2009. The last Glacial Maximum. *Science* 325, 710–714. <https://doi.org/10.1126/science.1172873>.
- Comas, M., Pinheiro, L.M., 2010. The Melilla carbonate mounds: do deep-water coral mounds count on seeping fluids in the Alboran Sea? *Rapp. Comm. int. Mer Médit.* 39.
- Corbera, G., Lo Iacono, C., Gràcia, E., Grinyó, J., Pierdomenico, M., Huvenne, V.A.I., Aguilar, R., Gili, J.M., 2019. Ecological characterisation of a Mediterranean cold-water coral reef: Cabliers Coral Mound Province (Alboran Sea, western Mediterranean). *Prog. Oceanogr.* 175, 245–262. <https://doi.org/10.1016/j.pocean.2019.04.010>.
- Corbera, G., Lo Iacono, C., Standish, C.D., Anagnostou, E., Titschack, J., Katsamenis, O., Cacho, I., Van Rooij, D., Huvenne, V.A.I., Foster, G.L., 2021. Glacio-eustatic variations and Sapropel events as main controls on the Middle Pleistocene-Holocene evolution of the Cabliers Coral Mound Province (W Mediterranean). *Quat. Sci. Rev.* <https://doi.org/10.1016/j.quascirev.2020.106783>.
- Davies, A.J., Guinotte, J.M., 2011. Global Habitat Suitability for Framework-Forming Cold-Water Corals. *PLoS One* 6, e18483. <https://doi.org/10.1371/journal.pone.0018483>.
- De la Torre, A., Serrano, A., Fernández-Salas, L.M., García, M., Aguilar, R., 2018. Identifying epibenthic habitats on the Seco de los Olivos Seamount: Species assemblages and environmental characteristics. *Deep. Res. Part I Oceanogr. Res. Pap.* 135, 9–22. <https://doi.org/10.1016/j.dsr.2018.03.015>.
- De Nooijer, L.J., Brombacher, A., Mewes, A., Langer, G., Nehrke, G., Bijma, J., Reichart, G.J., 2017. Ba incorporation in benthic foraminifera. *Biogeosciences* 14. <https://doi.org/10.5194/bg-14-3387-2017>.
- DeGeest, A.L., Mullenbach, B.L., Puig, P., Nittrouer, C.A., Drexler, T.M., Durrieu de Madron, X., Orange, D.L., 2008. Sediment accumulation in the western Gulf of Lions, France: the role of Cap de Creus Canyon in linking shelf and slope sediment dispersal systems. *Cont. Shelf Res.* 28, 2031–2047. <https://doi.org/10.1016/j.csr.2008.02.008>.
- Di Stefano, A., Foresi, L.M., Incarbona, A., Sprovieri, M., Vallefucio, M., Iorio, M., Pelosi, N., Di Stefano, E., Sangiorgi, P., Budillon, F., 2015. Mediterranean coccolith ecobiostatigraphy since the penultimate Glacial (the last 145,000 years) and ecobioevent traceability. *Mar. Micropaleontol.* 115, 24–38. <https://doi.org/10.1016/j.marmicro.2014.12.002>.
- Dinarès-Turell, J., Hoogakker, B.A.A., Roberts, A.P., Rohling, E.J., Sagnotti, L., 2003. Quaternary climatic control of biogenic magnetite production and eolian dust input in cores from the Mediterranean Sea. *Palaeogeogr. Palaeoclimatol. Palaeoecol.* 190, 195–209. [https://doi.org/10.1016/S0031-0182\(02\)00605-3](https://doi.org/10.1016/S0031-0182(02)00605-3).
- Dodds, L.A., Roberts, J.M., Taylor, A.C., Marubini, F., 2007. Metabolic tolerance of the cold-water coral *Lophelia pertusa* (Scleractinia) to temperature and dissolved oxygen change. *J. Exp. Mar. Biol. Ecol.* 349, 205–214.
- Dorschel, B., Hebbeln, D., Rüggeberg, A., Dullo, W.C., Freiwald, A., 2005. Growth and erosion of a cold-water coral covered carbonate mound in the Northeast Atlantic during the late Pleistocene and Holocene. *Earth Planet. Sci. Lett.* 233, 33–44. <https://doi.org/10.1016/j.epsl.2005.01.035>.
- D'Ortenzio, F., Ribera d'Alcalá, M., 2009. On the trophic regimes of the Mediterranean Sea: a satellite analysis. *Biogeosciences* 6, 139–148.
- Drake, J.L., Guillermin, M., Eagle, R.A., Jacobs, D.K., 2021. Fossil Corals with various Degrees of Preservation can Retain Information about Biomineralization-Related Organic Material. *Front. Earth Sci.* 9 <https://doi.org/10.3389/feart.2021.643864>.
- Du Preez, C., Swan, K.D., Curtis, J.M.R., 2020. Cold-water corals and other vulnerable biological structures on a North Pacific Seamount after half a Century of Fishing. *Front. Mar. Sci.* 7, 17. <https://doi.org/10.3389/fmars.2020.00017>.
- Dubois-Dauphin, Q., Montagna, P., Siani, G., Douville, E., Wienberg, C., Hebbeln, D., Liu, Z., Kallel, N., Dapigny, A., Revel, M., Pons-Branchu, E., Taviani, M., Colin, C., 2017. Hydrological variations of the intermediate water masses of the western Mediterranean Sea during the past 20 ka inferred from neodymium isotopic composition in foraminifera and cold-water corals. *Clim. Past* 13, 17–37. <https://doi.org/10.5194/cp-13-17-2017>.
- Duineveld, G.C.A., Jeffreys, R.M., Lavaley, M.S.S., Davies, A.J., Bergman, M.J.N., Watmough, T., Witbaard, R., 2012. Spatial and tidal variation in food supply to

- shallow cold-water coral reefs of the Mingulay Reef complex (Outer Hebrides, Scotland). *Mar. Ecol. Prog. Ser.* 444, 97–115.
- Eggs, S.M., Grün, R., McCulloch, M.T., Pike, A.W.G., Chappell, J., Kinsley, L., Mortimer, G., Shelley, M., Murray-Wallace, C.V., Spötl, C., Taylor, L., 2005. In situ U-series dating by laser-ablation multi-collector ICPMS: New prospects for Quaternary geochronology. *Quat. Sci. Rev.* 24, 2523–2538. <https://doi.org/10.1016/j.quascirev.2005.07.006>.
- Eisele, M., Frank, N., Wienberg, C., Hebbeln, D., López Correa, M., Douville, E., Freiwald, A., 2011. Productivity controlled cold-water coral growth periods during the last glacial off Mauritania. *Mar. Geol.* 280, 143–149. <https://doi.org/10.1016/j.margeo.2010.12.007>.
- Fabri, M.-C., Pedel, L., Beuck, L., Galgani, F., Hebbeln, D., Freiwald, A., 2014. Megafauna of vulnerable marine ecosystems in French Mediterranean submarine canyons: Spatial distribution and anthropogenic impacts. *Deep Sea Res. Part II Top. Stud. Oceanogr.* 104, 184–207.
- Fentimen, R., Feenstra, E., Rüggeberg, A., Vennemann, T., Hajdas, I., Adatte, T., Van Rooij, D., Foubert, A., 2020. Cold-water coral mound archive provides unique insights into intermediate water mass dynamics in the alboran sea during the last deglaciation. *Front. Mar. Sci.* 7 <https://doi.org/10.3389/fmars.2020.00354>.
- Ferjani, D., Gana, S., 2010. Seasonal circulation and mass flux estimates in the western Sicily Strait derived from a variational inverse section model. *Deep. Res. Part I Oceanogr. Res. Pap.* 57. <https://doi.org/10.1016/j.dsr.2010.07.007>.
- Flhailhearta, S.N., Reichart, G.J., Jorissen, F.J., Fontanier, C., Rohling, E.J., Thomson, J., De Lange, G.J., 2010. Reconstructing the seafloor environment during sapropel formation using benthic foraminiferal trace metals, stable isotopes, and sediment composition. *Paleoceanography* 25. <https://doi.org/10.1029/2009PA001869>.
- Fink, H.G., Wienberg, C., Hebbeln, D., McGregor, H.V., Schmiedl, G., Taviani, M., Freiwald, A., 2012. Oxygen control on Holocene cold-water coral development in the eastern Mediterranean Sea. *Deep. Res. Part I Oceanogr. Res. Pap.* 62, 89–96. <https://doi.org/10.1016/j.dsr.2011.12.013>.
- Fink, H.G., Wienberg, C., De Pol-Holz, R., Wintersteller, P., Hebbeln, D., 2013. Cold-water coral growth in the Alboran Sea related to high productivity during the late Pleistocene and Holocene. *Mar. Geol.* 339, 71–82.
- Fink, H.G., Wienberg, C., De Pol-Holz, R., Hebbeln, D., 2015. Spatio-temporal distribution patterns of Mediterranean cold-water corals (*Lophelia pertusa* and *Madrepora oculata*) during the past 14,000 years. *Deep. Res. Part I Oceanogr. Res. Pap.* 103, 37–48. <https://doi.org/10.1016/j.dsr.2015.05.006>.
- Flöter, S., Fietzke, J., Gutjahr, M., Farmer, J., Hönsich, B., Nehrke, G., Eisenhauer, A., 2019. The influence of skeletal micro-structures on potential proxy records in a bamboo coral. *Geochim. Cosmochim. Acta* 248. <https://doi.org/10.1016/j.gca.2018.12.027>.
- Fosså, J.H., Lindberg, B., Christensen, O., Lundålv, T., Svellingen, I., Mortensen, P.B., Alvsåvg, J., 2005. Mapping of *Lophelia* reefs in Norway: experiences and survey methods. In: *Cold-Water Corals and Ecosystems*. Springer-Verlag, pp. 359–391. [https://doi.org/10.1007/3-540-27673-4\\_18](https://doi.org/10.1007/3-540-27673-4_18).
- Frank, N., Paterne, M., Ayliffe, L., van Weering, T., Henriot, J.P., Blamart, D., 2004. Eastern North Atlantic deep-sea corals: Tracing upper intermediate water  $\Delta 14C$  during the Holocene. *Earth Planet. Sci. Lett.* 219 [https://doi.org/10.1016/S0012-821X\(03\)00721-0](https://doi.org/10.1016/S0012-821X(03)00721-0).
- Frank, N., Ricard, E., Lutringer-Paquet, A., van der Land, C., Colin, C., Blamart, D., Foubert, A., Van Rooij, D., Henriot, J.P., de Haas, H., van Weering, T., 2009. The Holocene occurrence of cold water corals in the NE Atlantic: Implications for coral carbonate mound evolution. *Mar. Geol.* 266, 129–142. <https://doi.org/10.1016/j.margeo.2009.08.007>.
- Frank, N., Freiwald, A., López Correa, M., Wienberg, C., Eisele, M., Hebbeln, D., Van Rooij, D., Henriot, J.P., Colin, C., van Weering, T., de Haas, H., Buhl-Mortensen, P., Roberts, J.M., De Mol, B., Douville, E., Blamart, D., Hatté, C., 2011. Northeastern Atlantic cold-water coral reefs and climate. *Geology* 39, 743–746. <https://doi.org/10.1130/G31825.1>.
- Freiwald, A., Beuck, L., Rüggeberg, A., Taviani, M., Hebbeln, D., R/V Meteor Cruise M70–1 participants, 2009. The white coral community in the Central Mediterranean Sea revealed by ROV surveys. *Oceanography* 22, 58–74.
- Gana, S., Iudicone, D., Ghenim, L., Mortier, L., Testor, P., Tintore, J., Olita, A., 2015. Monitoring water masses properties by Glider in Sardinia Channel during summer 2014. *Geophys. Res. Abstr.* 17.
- Glock, N., Eisenhauer, A., Liebetrau, V., Wiedenbeck, M., Hensen, C., Nehrke, G., 2012. EMP and SIMS studies on Mn/Ca and Fe/Ca systematics in benthic foraminifera from the Peruvian OMZ: a contribution to the identification of potential redox proxies and the impact of cleaning protocols. *Biogeosciences* 9. <https://doi.org/10.5194/bg-9-341-2012>.
- Gori, A., Orejas, C., Madurell, T., Bramanti, L., Martins, M., Quintanilla, E., Marti-Puig, P., Iacono, C., Lo Puig, P., Requena, S., et al., 2013. Bathymetrical distribution and size structure of cold-water coral populations in the Cap de Creus and Lacaze-Duthiers canyons (northwestern Mediterranean). *Biogeosciences* 10, 2049–2060.
- Grant, K.M., Rohling, E.J., Bronk Ramsey, C., Cheng, H., Edwards, R.L., Florindo, F., Heslop, D., Marra, F., Roberts, A.P., Tamisieva, M.E., Williams, F., 2014. Sea-level variability over five glacial cycles. *Nat. Commun.* 5, 1–9. <https://doi.org/10.1038/ncomms6076>.
- Hall, J.M., Chan, L.H., 2004. Ba/Ca in *Neogloboquadrina pachyderma* as an indicator of deglacial meltwater discharge into the western Arctic Ocean. *Paleoceanography* 19. <https://doi.org/10.1029/2003PA000910>.
- Hebbeln, D., 2019. Highly Variable Submarine Landscapes in the Alborán Sea created by Cold-Water Corals. In: Orejas, C., Jiménez, C. (Eds.), *Mediterranean Cold-Water Corals: Past, Present and Future*. Springer, Cham, pp. 61–65. [https://doi.org/10.1007/978-3-319-91608-8\\_8](https://doi.org/10.1007/978-3-319-91608-8_8).
- Hemings, F., Te Hsieh, Y., Bridgestock, L., Spooner, P.T., Robinson, L.F., Frank, N., Henderson, G.M., 2018. Barium isotopes in cold-water corals. *Earth Planet. Sci. Lett.* 491 <https://doi.org/10.1016/j.epsl.2018.03.040>.
- Henehan, M.J., Foster, G.L., Rae, J.W.B., Prentice, K.C., Erez, J., Bostock, H.C., Marshall, B.J., Wilson, P.A., 2015. Evaluating the utility of B/Ca ratios in planktic foraminifera as a proxy for the carbonate system: a case study of Globigerinoides ruber. *Geochim. Geophys. Geosyst.* 16 <https://doi.org/10.1002/2014GC005514>.
- Henry, L.-A., Roberts, J.M., 2007. Biodiversity and ecological composition of macrobenthos on cold-water coral mounds and adjacent off-mound habitat in the bathyal Porcupine Seabight, NE Atlantic. *Deep Sea Res. Part I Oceanogr. Res. Pap.* 54, 654–672.
- Hillier, S., 2000. Accurate quantitative analysis of clay and other minerals in sandstones by XRD: comparison of a Rietveld and a reference intensity ratio (RIR) method and the importance of sample preparation. *Clay Miner.* 35 <https://doi.org/10.1180/000985500546666>.
- Hoffmann, J., Bahr, A., Voigt, S., Schönfeld, J., Nürnberg, D., Rethemeyer, J., 2014. Disentangling abrupt deglacial hydrological changes in northern South America: Insolation versus oceanic forcing. *Geology* 42, 579–582. <https://doi.org/10.1130/G35562.1>.
- Huh, Y., Chan, L.H., Zhang, L., Edmond, J.M., 1998. Lithium and its isotopes in major world rivers: implications for weathering and the oceanic budget. *Geochim. Cosmochim. Acta* 62, 2039–2051. [https://doi.org/10.1016/S0016-7037\(98\)00126-4](https://doi.org/10.1016/S0016-7037(98)00126-4).
- Incarbona, A., Di Stefano, E., Parti, B., Pelosi, N., Bonomo, S., Mazzola, S., Sprovieri, R., Tranchida, G., Zgozi, S., Bonanno, A., 2008. Holocene millennial-scale productivity variations in the Sicily Channel (Mediterranean Sea). *Paleoceanography* 23. <https://doi.org/10.1029/2007PA001581>.
- Jacquet, S.H.M., Monnin, C., Riou, V., Jullion, L., Tanhua, T., 2016. A high resolution and quasi-zonal transect of dissolved Ba in the Mediterranean Sea. *Mar. Chem.* 178, 1–7. <https://doi.org/10.1016/j.marchem.2015.12.001>.
- Jaffey, A.H., Flynn, K.F., Glendenin, L.E., Bentley, W.C., Essling, A.M., 1971. Precision measurement of half-lives and specific activities of U235 and U238. *Phys. Rev. C* 4, 1889–1906. <https://doi.org/10.1103/PhysRevC.4.1889>.
- Jouini, M., Béranger, K., Arsouze, T., Beuvier, J., Thiria, S., Crépon, M., Taupier-Letage, I., 2016. The Sicily Channel surface circulation revisited using a neural clustering analysis of a high-resolution simulation. *J. Geophys. Res. Ocean.* 121, 4545–4567. <https://doi.org/10.1002/2015JC011472>.
- Kampman, N., Burnside, N.M., Shipton, Z.K., Chapman, H.J., Nicholl, J.A., Ellam, R.M., Bickle, M.J., 2012. Pulses of carbon dioxide emissions from intracrustal faults following climatic warming. *Nat. Geosci.* 5, 352–358. <https://doi.org/10.1038/ngeo1451>.
- Kano, A., Ferdelman, T.G., Williams, T., Henriot, J.-P., Ishikawa, T., Kawagoe, N., Takashima, C., Kakizaki, Y., Abe, K., Sakai, S., et al., 2007. Age constraints on the origin and growth history of a deep-water coral mound in the Northeast Atlantic drilled during Integrated Ocean Drilling Program Expedition 307. *Geology* 35, 1051–1054.
- Krengel, T., 2020. 550,000 Years of Marine Climate Variability in the Western Mediterranean Sea Revealed by Cold-Water Corals. *Diss. Univ. Heidelberg*.
- Lambeck, K., Rouby, H., Purcell, A., Sun, Y., Sambridge, M., 2014. Sea level and global ice volumes from the Last Glacial Maximum to the Holocene. *Proc. Natl. Acad. Sci. U. S. A.* 111, 15296–15303. <https://doi.org/10.1073/pnas.1411762111>.
- Lea, D., Boyle, E., 1989. Barium content of benthic foraminifera controlled by bottom-water composition. *Nature* 338. <https://doi.org/10.1038/338751a0>.
- Lea, D.W., Boyle, E.A., 1990. A 210,000-year record of barium variability in the deep Northwest Atlantic Ocean. *Nature* 347. <https://doi.org/10.1038/347269a0>.
- Lea, D.W., Spero, H.J., 1994. Assessing the reliability of paleochemical tracers: Barium uptake in the shells of planktonic foraminifera. *Paleoceanography* 9. <https://doi.org/10.1029/94PA00151>.
- Lea, D.W., Shen, G.T., Boyle, E.A., 1989. Coralline barium records temporal variability in equatorial Pacific upwelling. *Nature* 340. <https://doi.org/10.1038/340373a0>.
- Lisiecki, L.E., Raymo, M.E., 2005. A Pliocene-Pleistocene stack of 57 globally distributed benthic  $\delta^{18}O$  records. *Paleoceanography* 20, 1–17. <https://doi.org/10.1029/2004PA001071>.
- Lo Iacono, C., Gràcia, E., Ranero, C.R., Emelianov, M., Huvenne, V.A.I., Bartolomé, R., Booth-Rea, G., Prades, J., Ambroso, S., Dominguez, C., et al., 2014. The West Melilla cold water coral mounds, Eastern Alboran Sea: Morphological characterization and environmental context. *Deep Sea Res. Part II Top. Stud. Oceanogr.* 99, 316–326.
- Lo Iacono, C., Gracia, E., Agnastounou, E., Emelianov, M., Foster, G.L., Garcia-Ladona, E., Gili, J.M., Grinyo, J., Huvenne, V.A.I., Kastamemis, O.L., Mavrogordato, M.N., Perea, H., Pierdomenico, M., Vertino, A., Victorero-Gonzalez, L., Van Rooij, D., 2016. Living reefs and DWC mounds in the Alboran Sea (Western Mediterranean): Holocene evolution and present-day conditions. In: 6 International Symposium on Deep-Sea Corals, 11.09.-16.09.2016. Boston, USA.
- Lo Iacono, C., Savini, A., Basso, D., 2018. Cold-water carbonate bioconstructions. In: *Submarine Geomorphology*. Springer, pp. 425–455.
- Locarnini, M., Mishonov, A., Baranova, O., Boyer, T., Zweng, M., Garcia, H., Reagan, J., Seidov, D., Weathers, K., Paver, C., Smolyar, I., 2018. *World Ocean Atlas 2018, Volume 1: Temperature*.
- López Correa, M., Montagna, P., Joseph, N., Rüggeberg, A., Fietzke, J., Flögel, S., Dorschel, B., Goldstein, S.L., Wheeler, A., Freiwald, A., 2012. Preboreal onset of cold-water coral growth beyond the Arctic Circle revealed by coupled radiocarbon and U-series dating and neodymium isotopes. *Quat. Sci. Rev.* 34, 24–43. <https://doi.org/10.1016/j.quascirev.2011.12.005>.
- Lopez-Fernandez, P., Calafat, A., Sanchez-Vidal, A., Canals, M., Mar Flexas, M., Cateura, J., Company, J.B., 2013. Multiple drivers of particle fluxes in the Blanes

- submarine canyon and southern open slope: results of a year round experiment. *Prog. Oceanogr.* 118, 95–107. <https://doi.org/10.1016/j.pocan.2013.07.029>.
- Maher, B.A., Prospero, J.M., Mackie, D., Gaiero, D., Hesse, P.P., Balkanski, Y., 2010. Global connections between aeolian dust, climate and ocean biogeochemistry at the present day and at the last glacial maximum. *Earth-Sci. Rev.* <https://doi.org/10.1016/j.earscirev.2009.12.001>.
- Maier, C., Hegeman, J., Weinbauer, M.G., Gattuso, J.-P., 2009. Calcification of the cold-water coral *Lophelia pertusa*, under ambient and reduced pH. *Biogeosciences* 6, 1671–1680.
- Maina, J., de Moel, H., Vermaat, J.E., Henrich Bruggemann, J., Guillaume, M.M.M., Grove, C.A., Madin, J.S., Mertz-Kraus, R., Zinke, J., 2012. Linking coral river runoff proxies with climate variability, hydrology and land-use in Madagascar catchments. *Mar. Pollut. Bull.* 64 <https://doi.org/10.1016/j.marpolbul.2012.06.027>.
- Mangini, A., Godoy, J.M., Godoy, M.L., Kowsmann, R., Santos, G.M., Ruckelshausen, M., Schroeder-Ritzrau, A., Wacker, L., 2010. Deep sea corals off Brazil verify a poorly ventilated Southern Pacific Ocean during H2, H1 and the Younger Dryas. *Earth Planet. Sci. Lett.* 293 <https://doi.org/10.1016/j.epsl.2010.02.041>.
- Manzella, G.M.R., Hopkins, T.S., Minnett, P.J., Nacini, E., 1990. Atlantic water in the strait of Sicily. *J. Geophys. Res.* 95, 1569. <https://doi.org/10.1029/JC095iC02p01569>.
- Marchitto, T.M., Bryan, S.P., Doss, W., McCulloch, M.T., Montagna, P., 2018. A simple biomineralization model to explain Li, Mg, and Sr incorporation into aragonitic foraminifera and corals. *Earth Planet. Sci. Lett.* 481 <https://doi.org/10.1016/j.epsl.2017.10.022>.
- Marsay, C.M., Sanders, R.J., Henson, S.A., Pabortsava, K., Achterberg, E.P., Lampitt, R.S., 2015. Attenuation of sinking particulate organic carbon flux through the mesopelagic ocean. *Proc. Natl. Acad. Sci. U. S. A.* 112, 1089–1094. <https://doi.org/10.1073/pnas.1415311112>.
- Martínez-Díaz, A., Pelejero, C., Cobacho, S., Movilla, J., Dinarès-Turell, J., Calvo, E., 2021. A 1-million-year record of environmental change in the Central Mediterranean Sea from organic molecular proxies. *Paleoceanogr. Paleoclimatol.* 36 <https://doi.org/10.1029/2021PA004289>.
- Martorelli, E., Petroni, G., Chiocci, F.L., et al., 2011. Contourites offshore Pantelleria Island (Sicily Channel, Mediterranean Sea): depositional, erosional and biogenic elements. *Geo-Marine Lett.* 31, 481–493.
- Masce, G.H., Tricart, P., Torelli, L., Bouillin, J.P., Rolfo, F., Lapiere, H., Monié, P., Depardon, S., Masce, L., Peis, D., 2001. Evolution of the Sardinia Channel (Western Mediterranean): New constraints from a diving survey on Cornacya seamount off SE Sardinia. *Mar. Geol.* 179, 179–201. [https://doi.org/10.1016/S0025-3227\(01\)00220-1](https://doi.org/10.1016/S0025-3227(01)00220-1).
- Matos, L., Wienberg, C., Titschack, J., Schmiedl, G., Frank, N., Abrantes, F., Cunha, M.R., Hebbeln, D., 2017. Coral mound development at the Campeche cold-water coral province, southern Gulf of Mexico: Implications of Antarctic Intermediate Water increased influence during interglacials. *Mar. Geol.* 392, 53–65. <https://doi.org/10.1016/j.margeo.2017.08.012>.
- McCulloch, M., Fallon, S., Wyndham, T., Hendy, E., Lough, J., Barnes, D., 2003. Coral record of increased sediment flux to the inner Great Barrier Reef since European settlement. *Nature* 421. <https://doi.org/10.1038/nature01361>.
- McCulloch, M., Taviani, M., Montagna, P., López Correa, M., Remia, A., Mortimer, G., 2010. Proliferation and demise of deep-sea corals in the Mediterranean during the Younger Dryas. *Earth Planet. Sci. Lett.* 298, 143–152. <https://doi.org/10.1016/j.epsl.2010.07.036>.
- McGregor, H.V., Hellstrom, J., Fink, D., Hua, Q., Woodroffe, C.D., 2011. Rapid U-series dating of young fossil corals by laser ablation MC-ICPMS. *Quat. Geochronol.* 6, 195–206. <https://doi.org/10.1016/j.quageo.2010.10.002>.
- McManus, M., Alldredge, A., Barnard, A., Boss, E., Case, J., Cowles, T., Donaghay, P., Eisner, L., Gifford, D., Greenlaw, C., Herren, C., Holliday, D., Johnson, D., MacIntyre, S., McGehee, D., Osborn, T., Perry, M., Pieper, R., Rines, J., Smith, D., Sullivan, J., Talbot, M., Twardowski, M., Weidemann, A., Zaneveld, J., 2003. Characteristics, distribution and persistence of thin layers over a 48 hour period. *Mar. Ecol. Prog. Ser.* 261, 1–19. <https://doi.org/10.3354/meps261001>.
- Millot, C., 1999. Circulation in the Western Mediterranean Sea. *J. Mar. Syst.* 20, 423–442. [https://doi.org/10.1016/S0924-7963\(98\)00078-5](https://doi.org/10.1016/S0924-7963(98)00078-5).
- Montagna, P., Taviani, M., 2019. 11 Mediterranean Cold-Water Corals as Paleoclimate Archives. [https://doi.org/10.1007/978-3-319-91608-8\\_11](https://doi.org/10.1007/978-3-319-91608-8_11).
- Montagna, P., McCulloch, M., Douville, E., López Correa, M., Trotter, J., Rodolfo-Metalpa, R., Dissard, D., Ferrier-Pagès, C., Frank, N., Freiwald, A., Goldstein, S., Mazzoli, C., Reynaud, S., Rüggeberg, A., Russo, S., Taviani, M., 2014. Li/Mg systematics in scleractinian corals: Calibration of the thermometer. *Geochim. Cosmochim. Acta* 132, 288–310. <https://doi.org/10.1016/j.gca.2014.02.005>.
- Naumann, M.S., Orejas, C., Ferrier-Pagès, C., 2014. Species-specific physiological response by the cold-water corals *Lophelia pertusa* and *Madrepora oculata* to variations within their natural temperature range. *Deep. Res. Part II Top. Stud. Oceanogr.* 99, 36–41. <https://doi.org/10.1016/j.dsr2.2013.05.025>.
- Obaton, D., Millot, C., Chabert D'Hères, G., Taupier-Letage, I., 2000. The Algerian current: Comparisons between in situ and laboratory data sets. *Deep. Res. Part I Oceanogr. Res. Pap.* 47, 2159–2190. [https://doi.org/10.1016/S0967-0637\(00\)00014-5](https://doi.org/10.1016/S0967-0637(00)00014-5).
- Oguz, T., Macias, D., Garcia-Lafuente, J., Pascual, A., Tintore, J., 2014. Fueling plankton production by a meandering frontal jet: a case study for the Alboran Sea (Western Mediterranean). *PLoS One* 9, e111482.
- Onken, R., Robinson, A.R., Lermusiaux, P.F.J., Haley, P.J., Anderson, L.A., 2003. Data-driven simulations of synoptic circulation and transports in the Tunisia-Sardinia-Sicily region. *J. Geophys. Res. Ocean.* 108 [https://doi.org/10.1029/2002JC001348@10.1002/\(ISSN\)2169-9291.PBEMD1](https://doi.org/10.1029/2002JC001348@10.1002/(ISSN)2169-9291.PBEMD1).
- Orejas, C., Gori, A., Lo Iacono, C., Puig, P., Gili, J.-M., Dale, M.R.T., et al., 2009. Cold-water corals in the Cap de Creus canyon, northwestern Mediterranean: spatial distribution, density and anthropogenic impact. *Mar. Ecol. Prog. Ser.* 397, 37–51.
- Pearman, T.R.R., Robert, K., Callaway, A., Hall, R., Lo Iacono, C., Huvenne, V.A.I., 2020. Improving the predictive capability of benthic species distribution models by incorporating oceanographic data – Towards holistic ecological modelling of a submarine canyon. *Prog. Oceanogr.* 184, 102338 <https://doi.org/10.1016/j.pocan.2020.102338>.
- Price, D.M., Robert, K., Callaway, A., Lo Iacono, C., Hall, R.A., Huvenne, V.A.I., 2019. Using 3D photogrammetry from ROV video to quantify cold-water coral reef structural complexity and investigate its influence on biodiversity and community assemblage. *Coral Reefs* 38, 1007–1021. <https://doi.org/10.1007/s00338-019-01827-3>.
- Raddatz, J., Rüggeberg, A., 2021. Constraining past environmental changes of cold-water coral mounds with geochemical proxies in corals and foraminifera. *Depos. Rec.* <https://doi.org/10.1002/dep2.98>.
- Raddatz, J., Liebetrau, V., Rüggeberg, A., Hathorne, E., Krabbenhöft, A., Eisenhauer, A., Böhm, F., Vollstaedt, H., Fietzke, J., López Correa, M., Freiwald, A., Dullo, W.C., 2013. Stable Sr-isotope, Sr/Ca, Mg/Ca, Li/ca and Mg/Li ratios in the scleractinian cold-water coral *Lophelia pertusa*. *Chem. Geol.* 352 <https://doi.org/10.1016/j.chemgeo.2013.06.013>.
- Raddatz, J., Rüggeberg, A., Liebetrau, V., Foubert, A., Hathorne, E.C., Fietzke, J., Eisenhauer, A., Dullo, W.C., 2014. Environmental boundary conditions of cold-water coral mound growth over the last 3 million years in the Porcupine Seabight, Northeast Atlantic. *Deep. Res. Part II Top. Stud. Oceanogr.* 99 <https://doi.org/10.1016/j.dsr2.2013.06.009>.
- Raddatz, J., Liebetrau, V., Trotter, J., Rüggeberg, A., Flögel, S., Dullo, W.-C., Eisenhauer, A., Voigt, S., McCulloch, M., 2016. Environmental constraints on Holocene cold-water coral reef growth off Norway: Insights from a multiproxy approach. *Paleoceanography* 31, 1350–1367. <https://doi.org/10.1002/2016PA002974>.
- Remia, A., Taviani, M., 2005. Shallow-buried Pleistocene *Madrepora*-dominated coral mounds on a muddy continental slope, Tuscan Archipelago, NE Tyrrhenian Sea. *Facies* 50, 419–425.
- Rogers, A.D., 1999. The biology of *Lophelia pertusa* (Linnaeus 1758) and other deep-water reef-forming corals and impacts from human activities. *Int. Rev. Hydrobiol.* 84, 315–406.
- Rosenthal, Y., Field, M.P., Sherrell, R.M., 1999. Precise determination of element/calcium ratios in calcareous samples using sector field inductively coupled plasma mass spectrometry. *Anal. Chem.* 71 <https://doi.org/10.1021/ac981410x>.
- Roy-Barman, M., Pons-Branchu, E., Levier, M., Bordier, L., Foliot, L., Gdaniec, S., Ayrault, S., Garcia-Orellana, J., Masque, P., Castrillejo, M., 2019. Barium during the GEOTRACES GA-04S MedSea cruise: the Mediterranean Sea Ba budget revisited. *Chem. Geol.* 511, 431–440. <https://doi.org/10.1016/j.chemgeo.2018.09.015>.
- Rüggeberg, A., Dullo, C., Dorschel, B., Hebbeln, D., 2007. Environmental changes and growth history of a cold-water carbonate mound (Propeller Mound, Porcupine Seabight). *Int. J. Earth Sci.* 96, 57–72. <https://doi.org/10.1007/s00531-005-0504-1>.
- Savini, A., Corselli, C., 2010. High-resolution bathymetry and acoustic geophysical data from Santa Maria di Leuca Cold Water Coral province (Northern Ionian Sea—Apulian continental slope). *Deep Sea Res. Part II Top. Stud. Oceanogr.* 57, 326–344.
- Sinclair, D.J., 2005. Non-river flood barium signals in the skeletons of corals from coastal Queensland, Australia. *Earth Planet. Sci. Lett.* 237 <https://doi.org/10.1016/j.epsl.2005.06.039>.
- Sorgente, R., Olita, A., Oddo, P., Fazioli, L., Ribotti, A., 2011. Numerical simulation and decomposition of kinetic energy in the Central Mediterranean: insight on mesoscale circulation and energy conversion. *Ocean Sci.* 7, 503–519. <https://doi.org/10.5194/os-7-503-2011>.
- Soukissian, T., Karathanasi, F., Axaopoulos, P., Voukouvalas, E., Kotroni, V., 2018. Offshore wind climate analysis and variability in the Mediterranean Sea. *Int. J. Climatol.* <https://doi.org/10.1002/joc.5182>.
- Spooner, P.T., Chen, T., Robinson, L.F., Coath, C.D., 2016. Rapid uranium-series age screening of carbonates by laser ablation mass spectrometry. *Quat. Geochronol.* 31, 28–39. <https://doi.org/10.1016/j.quageo.2015.10.004>.
- Spooner, P.T., Robinson, L.F., Hemsing, F., Morris, P., Stewart, J.A., 2018. Extended calibration of cold-water coral Ba/Ca using multiple genera and co-located measurements of dissolved barium concentration. *Chem. Geol.* 499, 100–110. <https://doi.org/10.1016/j.chemgeo.2018.09.012>.
- Stalder, C., Vertino, A., Rosso, A., Rüggeberg, A., Pirkenseer, C., Spangenberg, J.E., Spezzaferrri, S., Camozzi, O., Rappo, S., Hajdas, I., 2015. Microfossils, a key to unravel cold-water carbonate mound evolution through time: evidence from the Eastern Alboran Sea. *PLoS One* 10. <https://doi.org/10.1371/journal.pone.0140223>.
- Stalder, C., El Kateb, A., Vertino, A., Rüggeberg, A., Camozzi, O., Pirkenseer, C.M., Spangenberg, J.E., Hajdas, I., Van Rooij, D., Spezzaferrri, S., 2018. Large-scale paleoceanographic variations in the western Mediterranean Sea during the last 34,000 years: from enhanced cold-water coral growth to declining mounds. *Mar. Micropaleontol.* 143, 46–62. <https://doi.org/10.1016/j.marmicro.2018.07.007>.
- Stansfield, K., Smeed, D.A., Gasparini, G., Pietro, McPhail, S., Millard, N., Stevenson, P., Webb, A., Vetrano, A., Rabe, B., 2001. Deep-sea, high-resolution, hydrography and current measurements using an autonomous underwater vehicle: the overflow from the Strait of Sicily. *Geophys. Res. Lett.* <https://doi.org/10.1029/2000GL012770>.
- Stewart, J.A., Robinson, L.F., Day, R.D., Strawson, I., Burke, A., Rae, J.W.B., Spooner, P. T., Samperiz, A., Etnoyer, P.J., Williams, B., Paytan, A., Leng, M.J., Häussermann, V., Wickes, L.N., Bratt, R., Pryer, H., 2020. Refining trace metal temperature proxies in cold-water scleractinian and stylasterid corals. *Earth Planet. Sci. Lett.* 545, 116412 <https://doi.org/10.1016/j.epsl.2020.116412>.

- Stewart, J.A., Li, T., Spooner, P.T., Burke, A., Chen, T., Roberts, J., Rae, J.W.B., Peck, V., Kender, S., Liu, Q., Robinson, L.F., 2021. Productivity and dissolved oxygen controls on the Southern ocean Deep-Sea Benthos during the Antarctic Cold Reversal. *Paleoceanogr. Paleoclimatol.* 36 <https://doi.org/10.1029/2021PA004288>.
- Tamborrino, L., Wienberg, C., Titschack, J., Wintersteller, P., Mienis, F., Schröder-Ritzrau, A., Freiwald, A., Orejas, C., Dullo, W.C., Haberkern, J., Hebbeln, D., 2019. Mid-holocene extinction of cold-water corals on the Namibian shelf steered by the Benguela oxygen minimum zone. *Geology* 47, 1185–1188. <https://doi.org/10.1130/G46672.1>.
- Taviani, M., Remia, A., Corselli, C., Freiwald, A., Malinverno, E., Mastrototaro, F., Savini, A., Tursi, A., 2005. First geo-marine survey of living cold-water *Lophelia* reefs in the Ionian Sea (Mediterranean basin). *Facies* 50, 409–417. <https://doi.org/10.1007/s10347-004-0039-0>.
- Taviani, M., Angeletti, L., Canese, S., Cannas, R., Cardone, F., Cau, A., Cau, A.B., Follesa, M.C., Marchese, F., Montagna, P., et al., 2017. The "Sardinian cold-water coral province" in the context of the Mediterranean coral ecosystems. *Deep Sea Res. Part II Top. Stud. Oceanogr.* 145, 61–78.
- Taviani, M., Angeletti, L., Fogliani, F., Corselli, C., Nasto, I., Pons-Branchu, E., Montagna, P., 2019. U/Th dating records of cold-water coral colonization in submarine canyons and adjacent sectors of the southern Adriatic Sea since the last Glacial Maximum. *Prog. Oceanogr.* 175, 300–308. <https://doi.org/10.1016/j.pocean.2019.04.011>.
- Toucanne, S., Jouet, G., Ducassou, E., Bassetti, M.A., Dennielou, B., Angue Minto'o, C.M., Lahmi, M., Touyet, N., Charlier, K., Lericolais, G., Mulder, T., 2012. A 130,000-year record of Levantine Intermediate Water flow variability in the Corsica Trough, western Mediterranean Sea. *Quat. Sci. Rev.* 33, 55–73. <https://doi.org/10.1016/j.quascirev.2011.11.020>.
- van Haren, H., 2014. Internal wave–zooplankton interactions in the Alboran Sea (W-Mediterranean). *J. Plankton Res.* 36, 1124–1134. <https://doi.org/10.1093/plankt/fbu031>.
- Wang, H., Lo Iacono, C., Wienberg, C., Titschack, J., Hebbeln, D., 2019. Cold-water coral mounds in the southern Alboran Sea (western Mediterranean Sea): Internal waves as an important driver for mound formation since the last deglaciation. *Mar. Geol.* 412, 1–18. <https://doi.org/10.1016/j.margeo.2019.02.007>.
- Wefing, A.M., Arps, J., Blaser, P., Wienberg, C., Hebbeln, D., Frank, N., 2017. High precision U-series dating of scleractinian cold-water corals using an automated chromatographic U and Th extraction. *Chem. Geol.* 475 <https://doi.org/10.1016/j.chemgeo.2017.10.036>.
- Wheeler, A.J., Beyer, A., Freiwald, A., de Haas, H., Huvenne, V.A.I., Kozachenko, M., Olu-Le Roy, K., Opderbecke, J., 2007. Morphology and environment of cold-water coral carbonate mounds on the NW European margin. *Int. J. Earth Sci.* 96, 37–56. <https://doi.org/10.1007/s00531-006-0130-6>.
- Wienberg, C., 2019. A deglacial cold-water coral boom in the Alborán sea: from coral mounds and species dominance. In: Orejas, C., Jiménez, C. (Eds.), *Mediterranean Cold-Water Corals: Past, Present and Future*. Springer, Cham, pp. 57–60. [https://doi.org/10.1007/978-3-319-91608-8\\_7](https://doi.org/10.1007/978-3-319-91608-8_7).
- Wienberg, C., Titschack, J., 2017. Framework-Forming Scleractinian Cold-Water Corals through Space and Time: A Late Quaternary North Atlantic Perspective, in: *Marine Animal Forests*. Springer, Cham, pp. 1–34. [https://doi.org/10.1007/978-3-319-17001-5\\_16-1](https://doi.org/10.1007/978-3-319-17001-5_16-1).
- Wienberg, C., Frank, N., Mertens, K.N., Stuut, J.B., Marchant, M., Fietzke, J., Mienis, F., Hebbeln, D., 2010. Glacial cold-water coral growth in the Gulf of Cádiz: Implications of increased palaeo-productivity. *Earth Planet. Sci. Lett.* 298, 405–416. <https://doi.org/10.1016/j.epsl.2010.08.017>.
- Wienberg, C., Titschack, J., Freiwald, A., Frank, N., Lundälv, T., Taviani, M., Beuck, L., Schröder-Ritzrau, A., Kregel, T., Hebbeln, D., 2018. The giant Mauritanian cold-water coral mound province: Oxygen control on coral mound formation. *Quat. Sci. Rev.* 185, 135–152. <https://doi.org/10.1016/j.quascirev.2018.02.012>.
- York, D., Evensen, N.M., Martínez, M.L., De Basabe Delgado, J., 2004. Unified equations for the slope, intercept, and standard errors of the best straight line. *Am. J. Phys.* 72, 367–375. <https://doi.org/10.1119/1.1632486>.
- Zweng, M., Reagan, J., Seidov, D., Boyer, T., Locarnini, M., Garcia, H., Mishonov, A., Baranova, O., Weathers, K., Paver, C., Smolyar, I., 2019. *World Ocean Atlas 2018, Volume 2: Salinity*.